

RL-TR-94-02
Final Technical Report
July 1994

AD-A284 056
■■■■■■■■■■



WAVEGUIDE SWITCHES USING ASYMMETRIC COUPLED QUANTUM WELLS

Martin Marietta Laboratories

Sponsored by
Advanced Research Projects Agency
ARPA Order No. 7318

DTIC
ELECTE
SEP 02 1994
S G D

APPROVED FOR PUBLIC RELEASE; DISTRIBUTION UNLIMITED

7928

94-28490

■■■■■■■■■■

The views and conclusions contained in this document are those of the authors and should not be interpreted as necessarily representing the official policies, either expressed or implied, of the Advanced Research Projects Agency or the U.S. Government.

Rome Laboratory
Air Force Materiel Command
Griffies Air Force Base, New York

DTIC QUALITY INSPECTED 1

94 9 01 085

This report has been reviewed by the Rome Laboratory Public Affairs Office (PA) and is releasable to the National Technical Information Service (NTIS). At NTIS it will be releasable to the general public, including foreign nations.

RL-TR-94-92 has been reviewed and is approved for publication.

APPROVED:

Richard A. Soref

RICHARD A. SOREF
Project Engineer

FOR THE COMMANDER:

Robert V. McGahan

ROBERT V. MCGAHAN
Acting Director
Electromagnetics & Reliability Directorate

If your address has changed or if you wish to be removed from the Rome Laboratory mailing list, or if the addressee is no longer employed by your organization, please notify RL (EROC) Hanscom AFB MA 01731. This will assist us in maintaining a current mailing list.

Do not return copies of this report unless contractual obligations or notices on a specific document require that it be returned.

WAVEGUIDE SWITCHES USING ASYMMETRIC COUPLED QUANTUM WELLS

Dr. Kenneth J. Ritter
Scott C. Horst

Contractor: Martin Marietta Laboratories
Contract Number: F19628-90-C-0028
Effective Date of Contract: 18 December 1989
Contract Expiration Date: 18 December 1993
Short Title of Work: Waveguide Switches using Asymmetric
Coupled Quantum Wells
Program Code Number: 2D10
Period of Work Covered: Dec 89 - Dec 93

Principal Investigator: Dr. Kenneth J. Ritter
Phone: (410) 204-2641

RL Project Engineer: Dr. Richard A. Soref
Phone: (617) 377-2380

Approved for public release; distribution unlimited.

This research was supported by the Advanced Research Projects Agency of the Department of Defense and was monitored by Richard A. Soref, RL (EROC), 80 Scott Drive, Hanscom AFB MA 01731-5000 under Contract F19628-90-C-0028.

Accession For	
NTIS CRA&I	<input checked="" type="checkbox"/>
DTIC TAB	<input type="checkbox"/>
Unannounced	<input type="checkbox"/>
Justification	
By	
Distribution /	
Availability Codes	
Dist	Avail and/or Special
A-1	

REPORT DOCUMENTATION PAGE			Form Approved OMB No. 0704-0188	
<small>Please request budget for this collection of information is estimated to average 1 hour per response, including the time for reviewing instructions, searching existing data sources, gathering and maintaining the data needed, and completing and reviewing this collection of information. Send comments regarding this burden estimate or any other aspect of this collection of information, including suggestions for reducing the burden, to Washington Headquarters Service, Directorate for Information Operations and Reports, 1215 Jefferson Davis Highway, Suite 1204, Arlington, VA 22202-4302, and to the Office of Management and Budget, Paperwork Reduction Project (0704-0188), Washington, DC 20503.</small>				
1. AGENCY USE ONLY (Leave Blank)		2. REPORT DATE July 1994		3. REPORT TYPE AND DATES COVERED Final Dec 89 - Dec 93
4. TITLE AND SUBTITLE WAVEGUIDE SWITCHES USING ASYMMETRIC COUPLED QUANTUM WELLS			5. FUNDING NUMBERS C - F19628-90-C-0028 PE - 62702F PR - 4600 TA - 19 WU - 80	
6. AUTHOR(S) Dr. Kenneth J. Ritter and Scott C. Horst				
7. PERFORMING ORGANIZATION NAME(S) AND ADDRESS(ES) Martin Marietta Laboratories 1450 So. Rolling Road Baltimore MD 21227			8. PERFORMING ORGANIZATION REPORT NUMBER N/A	
9. SPONSORING/MONITORING AGENCY NAME(S) AND ADDRESS(ES) Advanced Research Projects Agency 3701 North Fairfax Drive Arlington VA 22203-1714 Rome Laboratory (EROC) 80 Scott Rd Hanscom AFB MA 01731-2090			10. SPONSORING/MONITORING AGENCY REPORT NUMBER RL-TR-94-92	
11. SUPPLEMENTARY NOTES Rome Laboratory Project Engineer: Richard A. Soref/EROC/(717) 377-2390				
12a. DISTRIBUTION/AVAILABILITY STATEMENT Approved for public release; distribution unlimited.			12b. DISTRIBUTION CODE	
13. ABSTRACT (Maximum 200 words) This report contains the results of a three-year effort to investigate the use of Asymmetric Coupled Quantum Well in optical waveguide cross bar switches. The two types of devices investigated are the standard delta beta switch and the delta alpha switch. The delta alpha switch uses the imaginary part of the refractive index to modulate the intensity along different waveguide paths in the switch structure. Both types of switch were fabricated and tested. The delta beta switches produced are suitable as 1-input 2-output devices. The delta alpha switches were demonstrated as 2 by 2 cross bar switches with up to 40% throughput. To compensate for losses in the switches the use of amplifying elements was investigated. To provide gain at a longer wavelength than that of the excitons in the modulation waveguides, the quantum wells in the modulation waveguides were blue shifted using vacancy induced disordering (VID). The VID shifted quantum wells showed less Stark shift than the unshifted quantum wells. This effect is explained by the nearly parabolic shape of the disordered wells. Coupled quantum wells can be used to create a structure that will maintain a strongly Stark shifted spatially indirect transition even after VID. Modeling of the various waveguid structures used is also discussed.				
14. SUBJECT TERMS optical waveguides, optical switches, optical amplifiers quantum wells, GaAs, AlGaAs, vacancy-induced disordering			15. NUMBER OF PAGES 84	
			16. PRICE CODE	
17. SECURITY CLASSIFICATION OF REPORT UNCLASSIFIED	18. SECURITY CLASSIFICATION OF THIS PAGE UNCLASSIFIED	19. SECURITY CLASSIFICATION OF ABSTRACT UNCLASSIFIED	20. LIMITATION OF ABSTRACT U	

TABLE OF CONTENTS

TABLE OF CONTENTS.....	2
1. Introduction	4
1.1. Proposed Program.....	4
1.2. Summary of Results.....	5
1.3. Organization of this Report.....	6
2. General Waveguide Structures.....	6
2.1. Planar Waveguides	7
2.2. Etched Waveguides.....	8
2.3. Optical Measurement of Waveguides.....	9
3. Waveguide Modeling	9
3.1. Planar Waveguide Modeling.....	10
3.1.1. Effective Index Calculation	12
3.2. 2D Beam Propagator	13
3.3. Comparison of the Waveguide Models: Coupled Waveguide Calculations	15
3.3.1. Comparison of the Planar Waveguide Calculation and the Two Dimensional Beam Propagator Calculation.....	16
4. Optical Properties of Quantum Wells.....	18
4.1. Uncoupled Quantum Wells.....	18
4.2. Coupled Quantum Wells.....	18
5. Fabrication of Waveguide Structures.....	21
5.1. Photoresist Masking Process.....	21
5.2. Metal Mask Process.....	22
6. Coupled Waveguide Switch ($\Delta\beta$ Switch)	24
6.1. Theory of the $\Delta\beta$ Switch.....	24
6.1.1. Analytical Analysis of the $\Delta\beta$ Switch.....	25
6.2. Tolerance Analysis	26
6.2.1. Numerical Analysis of the $\Delta\beta$ Switch	28
6.3. 3-mm Long $\Delta\beta$ Switch	29
6.4. 500- μm Long $\Delta\beta$ Switch	35
7. The $\Delta\alpha$ Switch	39
7.1. $\Delta\alpha$ Waveguide Switch Structures	42
7.1.1. Waveguide Y-Splitters.....	43
7.1.2. Waveguide Crossovers	48
7.1.3. Waveguide Turning Mirrors.....	49
7.1.4. Curved waveguides	53
7.2. 2 x 2 $\Delta\alpha$ Switch without Gain	54
7.3. Using Disorder to Combine Gain and Modulation.....	57
7.3.1. Electrical Measurements on VID diodes.....	62
7.4. 2 x 2 Switch with Gain.....	63
7.4.1. Verification of Gain by Laser Measurements.....	66
7.4.2. Measurement of the $\Delta\alpha$ Switches with Gain	68
8. Conclusions.....	72

8.1. Results.....	72
8.2. Possible Variations and Extensions.....	73
9. References.....	74

1. Introduction

This report describes the results of a three-year study to explore the application of Asymmetric Coupled Quantum Well (ACQW) to waveguide switches. The ACQW structure and its electrooptic properties were developed and studied in an earlier program.¹ The program described here applied the resulting ACQW technology to two types of waveguide switch designs.

1.1. Proposed Program

The two types of switches studied in this program are shown schematically in Fig. 1 below. The first type of switch (Fig. 1a) is a $\Delta\beta$ switch. In this design, light enters one of the waveguide inputs (arrow) and is directed to one of a pair of parallel waveguides. The parallel waveguides are designed to evanescently couple such that light entering one of the guides will cross over to the other. In Fig. 1a, the light entering at the arrow on the left will emerge from the lower right output. To accomplish switching, a voltage is applied to V_{sw} . This causes a refractive index change in the electro-optic material comprising the waveguide so that the coupling between the two parallel guides is spoiled. The result is that the light no longer crosses over from one parallel guide to the other. With a bias applied to V_{sw} , light entering at the arrow (Fig. 1a) will emerge from the upper output on the right side of the switch. Because this switch uses the change in refractive index to change the propagation constant (β) of the waveguide it is generally referred to as a $\Delta\beta$ switch.

The second type of switch is shown in Fig. 1b. In this design, light entering one of the switch inputs is split equally into two paths so that it will emerge from both outputs of the switch. In this switch, application of a bias to V_{bar} (V_{cross}) causes the two bar (cross) paths to become opaque, so that light entering at the indicated input would then emerge only from the lower (upper) right output. Because of the loss inherent in the design of this switch (one half of the intensity is lost at each pass through a Y-splitter or combiner), gain sections must be added. Because this switch uses the change in the absorption coefficient (α) to accomplish switching, we refer to it as a $\Delta\alpha$ switch.

Both types are two input two output (2x2) cross-bar switches. This type of switch can be used as an element in a large switching network. As shown in Fig. 1c, six switches (represented as rectangles in the figure) can be configured to form a 4x4 switch network.

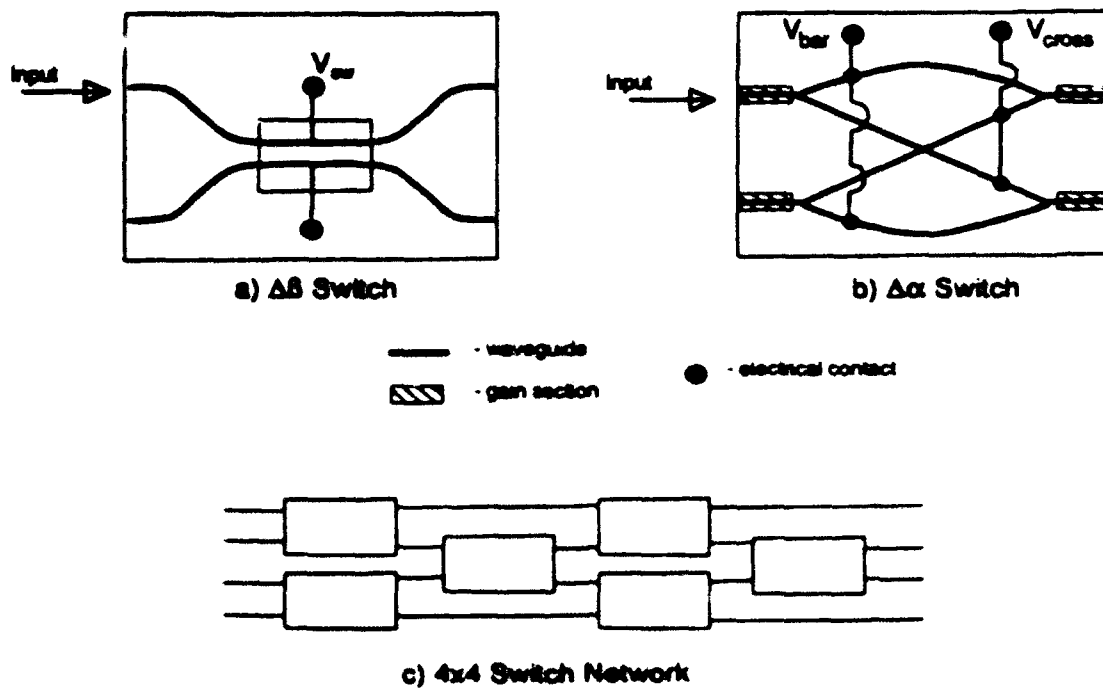


Figure 1. Schematic representation of the $\Delta\beta$ and $\Delta\alpha$ 2x2 cross-bar switches as well as a 4x4 switching network composed of six 2x2 cross-bar switches.

1.2. Summary of Results

Both $\Delta\alpha$ and $\Delta\beta$ switches were fabricated and tested in this program. Two designs of the $\Delta\beta$ switches, which included 3mm and 500 μ m cross-over lengths, were fabricated and tested with the results presented in section 6. The zero bias results of these switches were excellent, demonstrating that the models used accurately predicted the coupling between the waveguides, and that the fabrication techniques accurately produced the required waveguide dimensions. Under bias the predicted switching was observed, but electro-absorption in the waveguides made the switches asymmetric (i.e., light entering the bias guide behaved differently from light entering the unbiased guide). Because of this asymmetry, these switches could be used as one input two output switches, but not as 2x2 cross-bar switches.

The results of the $\Delta\alpha$ switch development are presented in section 7. This work successfully demonstrated all the properties required for the $\Delta\alpha$ switch. First, the various waveguide structures (e.g., Y-splitters, arcs and turning mirrors) were modeled, fabricated and successfully tested. A complete

switch structure without gain was fabricated and successfully tested. Finally, switches fabricated with vacancy induced disordering (VID) regions were fabricated to allow gain to be incorporated into the structures. These switches, while demonstrating gain, did not achieve high enough opacity in the reversed biased absorption waveguides to switch efficiently. This problem can be corrected by careful design of the ACQW structure so that it maintains the proper coupling after disordering.

1.3. Organization of this Report

Sections 2 to 5 of this report summarize general methods and techniques developed to design and fabricate the two types of switches studied in this program. Section 2 describes the optical waveguide structures, which consist of strip loaded waveguides formed over an epitaxially grown GaAs/Al_xGa_{1-x}As planar waveguide structure. The modeling of these waveguides is described in section 3. The electrooptic properties of the waveguides are produced by the quantum wells in the guiding layer of the planar waveguides. The optical properties of these quantum well structures are described in section 4. Section 5 describes the techniques used to fabricate the waveguide structures that form the switches. Because the structures and techniques were improved over the period of this program, the specific process used on an individual structure may have been different from that described in sections 2 to 5. In general, the specifics for a particular structure are described in the section dealing with that structure.

Sections 6 and 7 describe the design, fabrication and test results for the $\Delta\beta$ and $\Delta\alpha$ switches, respectively. Section 7 also includes discussions of each of the components of the $\Delta\alpha$ switch, which include Y-splitters, cross-overs, turning mirrors and arcs. Vacancy induced disordering for the purpose of blue shifting the quantum well excitons is also discussed in section 7.

Conclusions drawn from this work as well as recommendations for future work are presented in section 8.

2. General Waveguide Structures

The general form of the waveguide structure used throughout this program is shown in Fig. 2. The underlying planar waveguides are GaAs/AlGaAs structures grown epitaxially on GaAs substrates using molecular beam epitaxy (MBE). After growth, reactive ion etching (RIE) is used to create raised ridges on the surface of the planar waveguides forming strip-loaded waveguides. These structures provide both vertical and lateral confinement of the optical radiation.

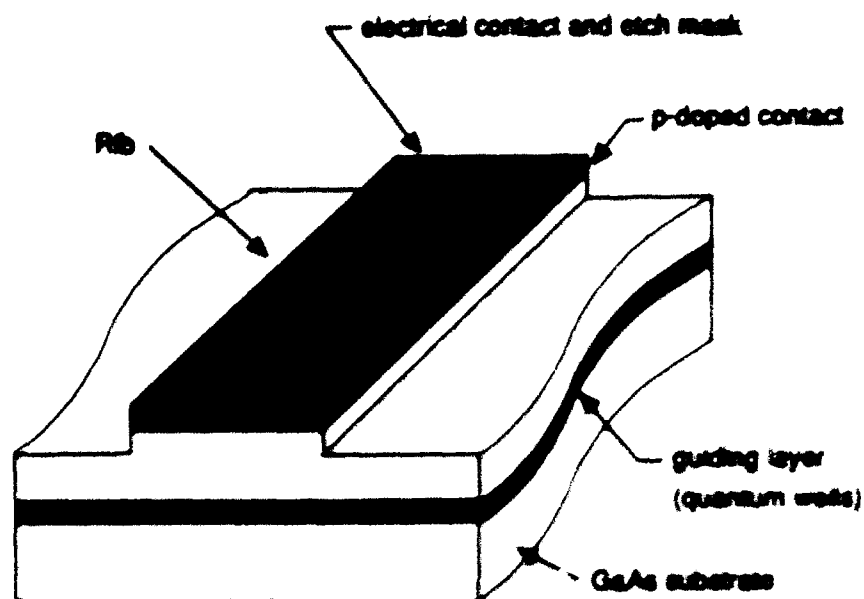


Figure 2. The basic waveguide structure used in both the $\Delta\beta$ and $\Delta\alpha$ switches. The underlying structure is a planar waveguide grown by molecular beam epitaxy. The rib formed by reactive ion etching provides lateral confinement of the optical mode

2.1. Planar Waveguides

The basic MBE-grown planar waveguide used in this program is shown in Fig. 3. The structure is a single mode planar waveguide created by first growing a series of layers totaling approximately $1.5\mu\text{m}$ thickness to form the lower cladding. This is followed by a guiding layer $0.2\mu\text{m}$ to $0.3\mu\text{m}$ thick with a refractive index 2.4% higher than that of the cladding. Finally, additional cladding was grown to form the complete planar waveguide structure. The quantum wells in the core of the planar waveguide provide the electrooptic characteristics of the device as described in section 4. The doping of the device, n-doped substrate, intrinsic planar waveguide, and p-doped cap, forms a p-i-n diode. For modulation, i.e., transforming a waveguide from transparent to opaque, a negative bias is applied to the p-doped cap. The resulting electric field across the quantum wells produces a Stark shift in the quantum well absorption (see sec. 4) causing the absorption wavelength to red shift to the illumination wavelength and absorb the light passing into the waveguide. For gain, the waveguides are forward biased.

The intrinsic cladding is formed by a superlattice (SL). The SL cladding has an effective index of refraction 2.4% less than the MQW core of the waveguide. As well as forming part of the waveguide, the SL provides a means

for checking the layer thicknesses after growth via x-ray diffraction as described in section 6.3. To provide complete characterization of the layer thicknesses and compositions, a photoluminescence (PL) spectrum of the top $\text{Al}_x\text{Ga}_{1-x}\text{As}$ cladding (below the cap) is taken. As described in section 6.4, the PL measurement allows determination of the $\text{Al}_x\text{Ga}_{1-x}\text{As}$ composition. This information along with the SL period allows complete determination of the composition and layer thicknesses throughout the structure.

Cap	$p^+ 2 \times 10^{18}$	500Å GaAs
Doped cladding	$p^+ 2 \times 10^{18}$	2500Å $\text{Al}_{0.3}\text{Ga}_{0.7}\text{As}$
Intrinsic cladding	SL	$\left\{ \begin{array}{l} 85\text{Å } \text{Al}_{0.3}\text{Ga}_{0.7}\text{As} \\ 15\text{Å } \text{GaAs} \end{array} \right\} \times 60$
MQW layer (waveguide core)		$\left\{ \begin{array}{l} 100\text{Å } \text{Al}_{0.3}\text{Ga}_{0.7}\text{As} \\ 100\text{Å } \text{GaAs} \\ 25\text{Å } \text{Al}_{0.3}\text{Ga}_{0.7}\text{As} \\ 50\text{Å } \text{GaAs} \end{array} \right\} \times 10$
Intrinsic cladding	SL	$\left\{ \begin{array}{l} 85\text{Å } \text{Al}_{0.3}\text{Ga}_{0.7}\text{As} \\ 15\text{Å } \text{GaAs} \end{array} \right\} \times 40$
Doped cladding	$n^+ 2 \times 10^{18}$	$\left\{ \begin{array}{l} 85\text{Å } \text{Al}_{0.3}\text{Ga}_{0.7}\text{As} \\ 15\text{Å } \text{GaAs} \end{array} \right\} \times 110$
Buffer	$n^+ 2 \times 10^{18}$	5000Å GaAs
n^+ GaAs substrate		

Figure 3. Typical epitaxially grown planar waveguide structure.

2.2. Etched Waveguides

The planar waveguide structures grown by MBE provide only vertical confinement of the optical energy. To provide lateral confinement, further processing of the MBE-grown wafer is necessary to form strip-loaded waveguides (SLWG) on the surface of the wafer as shown in Fig. 2. In all the waveguides used in this program, the waveguide ridges were formed using RIE, though two different methods were used to accomplish this as described in sec. 5. The SLWG provides lateral confinement because the area under the ridge has higher effective index than the surrounding area, leading to confinement of the optical mode to a region near the SLWG. The near-field intensity distribution from one of these waveguides (2µm wide and 1mm long) is shown in Fig. 4, demonstrating the well defined single mode pattern of these guides. The

fabrication of these waveguides is described in section 5 and the modeling of them is described in section 3.

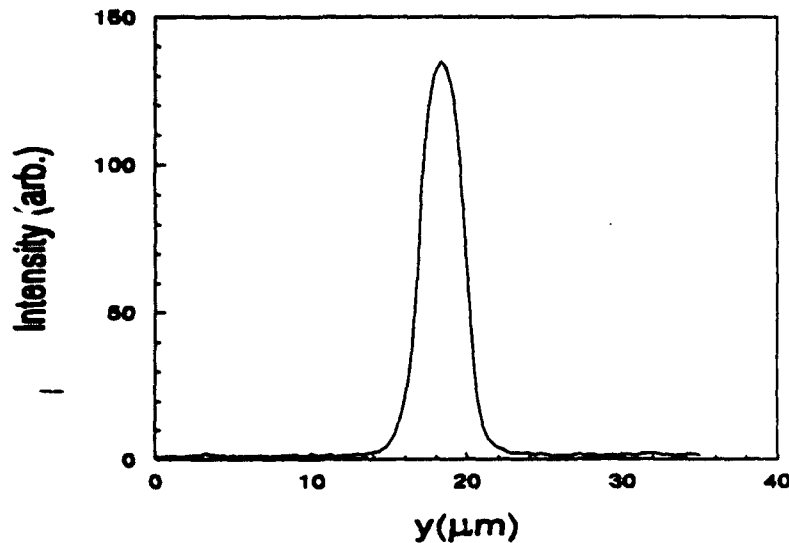


Figure 4. Near-field intensity distribution at the output of strip-loaded waveguide. The waveguide is $2\mu\text{m}$ wide by 1mm long.

2.3. Optical Measurement of Waveguides

Optical measurements of the waveguide structures were made by cleaving the waveguides and coupling into and out of the resulting facets using 20X, 0.4NA microscope objectives. The radiation source used was a Coherent 599 dye laser pumped by an argon ion laser running on all green lines. Depending on the measurement, output was monitored using single element Si photo diodes and/or a Pulnix Tm-540 CCD camera (with the AGC disabled). Output from the CCD camera was captured using a Colorado Video Inc. Video Frame Store 274D. The stored images could be transferred to a host computer for storage and further analysis.

3. Waveguide Modeling

The switch structures made in this program included evanescently coupled waveguides as well as various waveguide components such as : curves, Y-splitters, and turning mirrors. To properly design these structures it is necessary to be able to predict their performance mathematically. To do this we have used two general types of models. The first is based on a transfer matrix calculation that solves for optical modes in multi-layered structures. This model was used to calculate the modes of the planar waveguide structure and the

effective index of these structures as a function of upper cladding layer thickness. This model was also used to calculate modes of single straight SLWGs as well as coupling between pairs of straight SLWGs. The second model used is a 2 dimensional (2D) beam propagator. This model allows calculation of a mode propagating down a complex waveguide structure that may include curves, Y-splitters, curves, gaps, etc. Both models allow calculations that include complex refractive index values so that gain and loss can be modeled.

3.1. Planar Waveguide Modeling

As described in section 2, the underlying structure of all the waveguide devices presented in this report is a multi-layered planar structure grown using MBE. These structures can have hundreds of layers, which include the superlattice cladding, and the quantum well layers. To design the MBE growth, it is necessary to be able to calculate the modes of such a structure. To do this we use a transfer matrix technique that can calculate the optical electrical field distribution in all the layers of the structure as well as the complex propagation constant β . In our analysis, the geometry of the waveguide is set up as shown in Fig. 5. The y-component of the field is written in the exponential form of eq. E3.1-1.

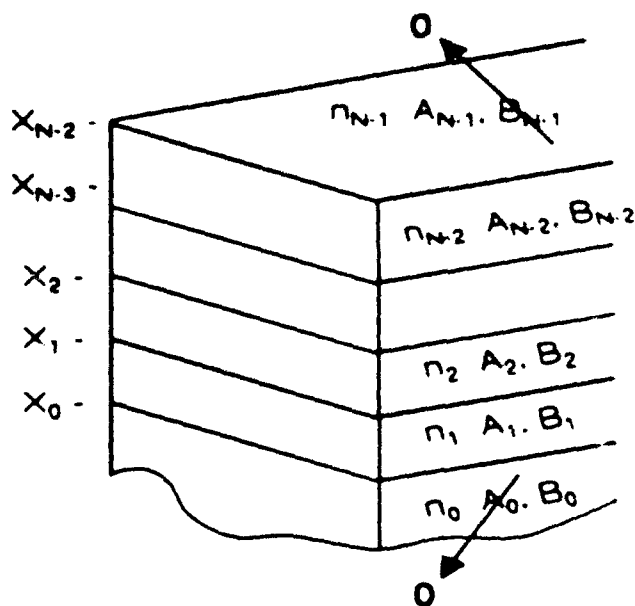


Figure 5. Geometry and layer indices used in the planar waveguide calculation.

$$E_x = A_j \cdot \exp(i\sqrt{n_j^2 \cdot k^2 - \beta^2} \cdot (x - x_j)) + B_j \cdot \exp(-i\sqrt{n_j^2 \cdot k^2 - \beta^2} \cdot (x - x_j)) \quad (\text{E3.1-1})$$

The boundary conditions require that at each interface between the layers of the waveguide the transverse components of the E and H fields be continuous. This leads to the relation given in E3.1-2 between the field coefficients in consecutive layers.

(E3.1-2)

$$\begin{bmatrix} A_{j+1} \\ B_{j+1} \end{bmatrix} = S_j \cdot \begin{bmatrix} A_j \\ B_j \end{bmatrix}$$

where:

$$S_j = \frac{1}{2 \cdot u_{j+1}} \begin{bmatrix} (u_j + u_{j+1}) \cdot R_j^+ & (u_{j+1} - u_j) \cdot R_j^- \\ (u_{j+1} - u_j) \cdot R_j^+ & (u_j + u_{j+1}) \cdot R_j^- \end{bmatrix}$$

$$u_j = \sqrt{n_j^2 \cdot k^2 - \beta^2} / m_j$$

$$m_j = \begin{cases} 1: TE \\ n_j^2: TM \end{cases}$$

$$R_j^\pm = \exp(\pm \sqrt{n_j^2 \cdot k^2 - \beta^2} \cdot D_j)$$

$$D_j = \begin{cases} x_j - x_{j+1}: j \neq 0 \\ 0: j = 0 \end{cases}$$

In these expressions, all quantities (except j and x) are complex. In a lossless guide the field coefficients (A_0 in the substrate and B_{N-1} in the capping layer) must be zero so that the field will decay exponentially in both cladding layers. To determine β , the calculation starts in the substrate with $A_0=0$ and calculates the coefficients A_j and B_j in each layer up to the cap. The value of B_{N-1} produced by this procedure is a function of β and for an arbitrary value of β will not be equal to zero as required by the boundary conditions. Values of β corresponding the waveguide modes are determined by applying the procedure

for different values of β , using a root finding routine to locate the complex values of β that satisfy the boundary condition $B_{N-1}(\beta)=0$.

The planar guides used here are actually leaky waveguides since the refractive index of the GaAs substrate is greater than or equal to the index of the waveguide core. For leaky modes, the field in the cladding is oscillatory, radiating through the cladding and substrate instead of exponentially decaying. The boundary condition in this case is that the coefficient of the inward propagating wave must be zero (i.e., the radiation escapes from the core so that at the last interface only an outward propagating wave is possible). Since the time dependence is given by $F_j(t)=F_j \cdot \exp(-i\omega t)$, the two terms in eq. 3.1-2 with coefficients A_{N-1} and B_{N-1} in the cap correspond to outgoing and incoming waves, respectively. Similarly, A_0 and B_0 correspond to incoming and outgoing waves respectively, in the substrate. The boundary conditions for a leaky waveguide are then: $A_0=0$ and $B_{N-1}=0$, which are the same as for a lossless guide. Hence the same procedure for determining β can be followed for a lossless guide or a guide that is leaky from either the cap or, the substrate, or both.

The program that performs this calculation reads the structure from an input file and then calculates the complex propagation constant for each waveguide mode found in the structure. The program is written so that any one of a number of parameters can be repeatedly incremented with the waveguide modes recalculated at each increment. The increment parameters include the wavelength, the refractive index of selected layers, and the thickness of selected layers. This is used to vary parameters of the guide to optimize layer thickness. In addition, the structure can be "etched" from the top by a desired increment. This is used to calculate the effective index (modal index) of the guide as a function of etch depth. This is important for designing the planar structure to work well with the etched waveguide structures.

3.1.1. Effective Index Calculation

In this program, all calculations of the laterally confined waveguide modes of the strip-loaded waveguides were made using effective index calculations. To calculate the effective index of our planar waveguide structures, we calculate the propagation constant of the fundamental mode and from it determine the modal index that is then used as the effective index of the guide. As material is removed from the upper cladding of the waveguide, the effective index decreases. Figure 6 shows an example calculation made using the planar waveguide program to calculate the effective index as a function of the amount of material etched from the top of the structure. The modal index is affected only weakly from about 0 to $0.4\mu\text{m}$ etch depth, beyond $0.4\mu\text{m}$ the modal index changes rapidly with etch depth.

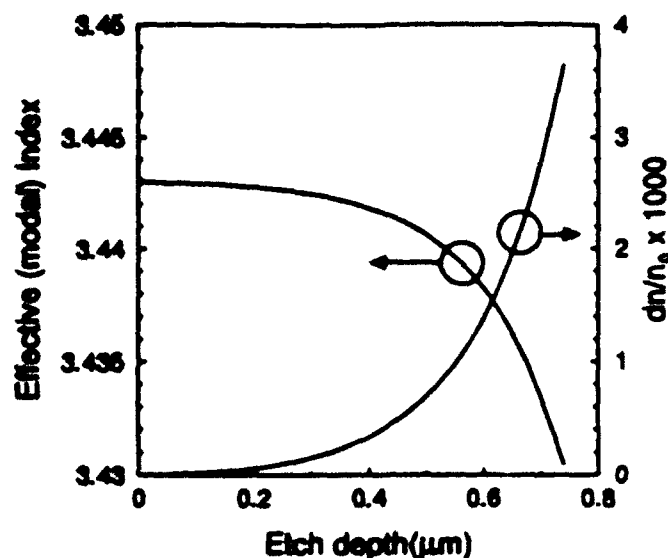


Figure 6. Calculated effective refractive index of a planar waveguide as a function of the thickness of material etched from the upper cladding layer.

3.2. 2D Beam Propagator

The planar waveguide calculation described in the last section (3.1) can be used to calculate the modes of a strip-loaded waveguide providing that the waveguide structure is independent of z (this includes multiple coupled guides that are parallel), where z is the direction of propagation. When the waveguide structure is more complicated and includes z -dependent structures, another analysis method must be used. We chose to use a 2D beam propagation calculation using methods described in a series of papers by Yevick et al.²⁻⁵. This method is based on the original technique described by J.A. Fleck,⁶ which starts with the scalar wave equation. Yevick's method uses a symmetrized split difference operator as shown in Eq. E3.2-1. The 2D beam propagator calculates the electric field E_j^n at equally spaced points (j) along a line (n). At step $n+1$, the field E_j^{n+1} is calculated along a line ($n+1$) spaced Δz from the last line.

$$\bar{E}^{n+1} = D_y \cdot e^{-i \frac{\Delta z}{2} \left(\frac{\partial^2}{\partial \alpha^2} - 1 \right)} \cdot D_y \cdot \bar{E}^n$$

$$D_\alpha = \frac{1 + \Delta_\alpha}{1 - \Delta_\alpha} \quad (\text{E3.2-1})$$

$$\Delta_\alpha = \frac{-i \cdot \Delta z}{8 \cdot k \cdot n_0} \cdot \frac{\partial^2}{\partial \alpha^2}$$

To evaluate this expression, define δE such that Eq. E3.2-2 is true.

$$D_\alpha E = \delta E - E \quad (\text{E3.2-2})$$

Equation E3.2-2 can then be rewritten as shown in Eq. E3.2-3.

$$(1 - \Delta_\alpha) \delta E = 2E \quad (\text{E3.2-3})$$

By approximating the second derivative as a divided difference, Eq. E3.2-1 becomes the matrix equation shown in Eq. E3.2-4.

$$\begin{pmatrix} \ddots & & & & \\ b & 1-2b & b & & \\ & b & 1-2b & b & \\ & & b & 1-2b & b \\ & & & \ddots & \ddots \end{pmatrix} \cdot \begin{pmatrix} \delta E_0 \\ \delta E_1 \\ \delta E_2 \\ \vdots \\ \delta E_N \end{pmatrix} = \begin{pmatrix} 2E_0 \\ 2E_1 \\ 2E_2 \\ \vdots \\ 2E_N \end{pmatrix} \quad (\text{E3.2-4})$$

$$\text{where: } b = \frac{i \cdot \Delta z}{8 \cdot k \cdot n_0 \cdot (\Delta \alpha)^2}$$

The matrix in Eq. E3.2-5 is tri-diagonal which can be solved using standard techniques.⁷ Once δE is determined, Eq. E3.2-2 is used to find $D_\alpha E$.

Once the procedure for evaluating $\Delta_\alpha E$ is established, the electric field distribution at step $n+1$ can be determined from the field at step n using equation E3.2-1.

The procedure for the beam propagator is:

1. Start with a solution at Z_0 (usually a Gaussian intensity distribution)
2. Operate with D_y (solve tri-diagonal matrix equation)
3. Multiply by the index phase term (only where $n \neq n_0$)

where the index phase term is given by E3.2-5

$$e^{-i \frac{n_g \cdot k}{2} \left\langle \frac{n^2}{n_0} - 1 \right\rangle \cdot \Delta z} \quad (\text{E3.2-5})$$

and the angle brackets $\langle \rangle$ denote the average from Z_n to Z_{n+1} .

4. Operate with Δ_x to get E_{n+1}
5. Increment n and return to step 1.

At each step, the calculation only uses the index profile along the lines Z_n and Z_{n+1} . Since we are using a 2D version of the beam propagation method, the refractive index of the guides is approximated using the effective index method.

3.3. Comparison of the Waveguide Models: Coupled Waveguide Calculations

As described above, two types of numerical models were used in this program, a planar waveguide transfer matrix calculation and a 2D beam propagator. To check the two models for consistency, we performed calculations on evanescently coupled waveguide structures using both techniques (the theory and calculations for coupled waveguides is described in detail in sec. 6.1). Though both of these models can be used to calculate the effects of evanescent coupling between two waveguides, the 2D beam propagator calculation is cumbersome for this type of calculation. The planar waveguide model that was originally written to design the MBE grown planar waveguides is actually better suited for this calculation (as described in sec. 6.2.1). The example calculations shown below demonstrate the consistency of the two models (at least for specific examples). Later comparisons between calculation and theory in sections 6.3 and 6.4 show that they match the measured results as well.

3.3.1. Comparison of the Planar Waveguide Calculation and the Two Dimensional Beam Propagator Calculation

The two waveguide calculation techniques would normally be used in different situations so that no direct comparison between the two methods would be possible. In the case of evanescently coupled waveguides however both methods can be used to calculate the coupling between the waveguides. This allows direct comparison between the two methods.

Figure 7 shows an example of the simplest form of evanescently coupled waveguide. This structure consists of two symmetric coupled waveguides running in parallel. This type of structure will always transfer all the radiation from one waveguide into the parallel waveguide after some length L_x . Also shown in the figure are the electric field distributions of the first two modes of the coupled waveguides. As described in section 3.1, the planar waveguide

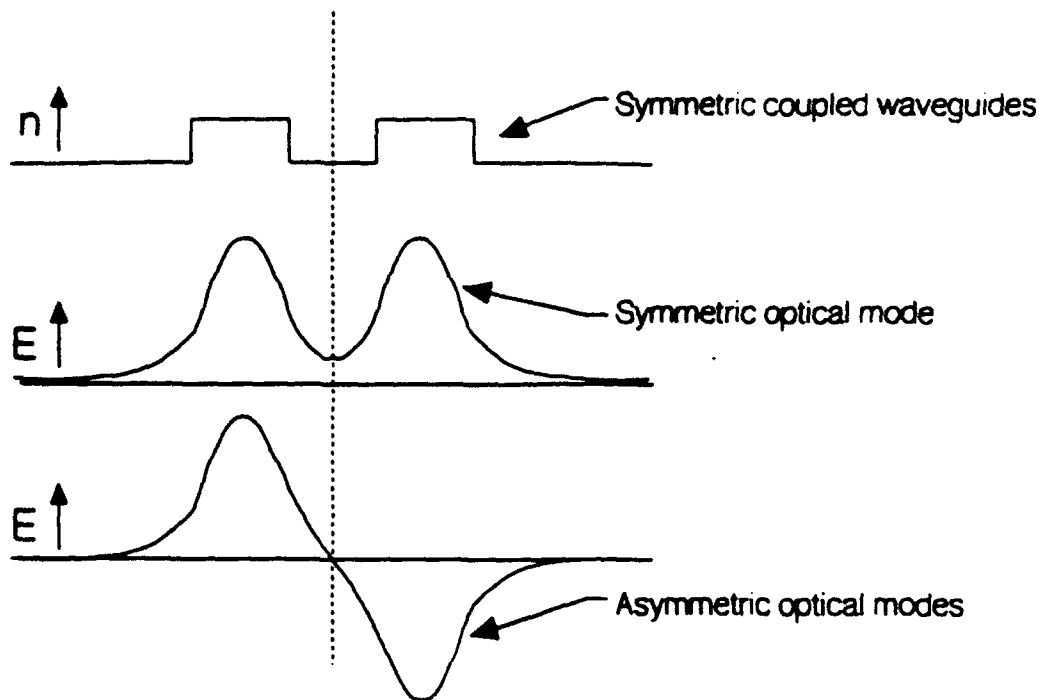


Figure 7. Cross-sectional view of symmetric coupled waveguides (top) and the electric field distributions of the first two optical modes.

calculation can be used to calculate these modes. This is accomplished under the effective index approximation by treating the cladding regions, waveguides, and the gap between waveguides as five layers with each layer having the effective index determined by the thickness of the upper cladding layer of its corresponding region. Once the first two waveguide modes have been

determined using the planar waveguide calculation the coupling length L_x can be determined from the difference in propagation constant between the two modes. For a pair of waveguides with widths=2.5 μm , separation=1.75 μm , cladding index=3.4 and waveguide index=3.4017 the planar waveguide calculation predicts a coupling length of $L_x=1.0\text{mm}$.

The same coupling calculation can be made with the beam propagator by starting a mode in one guide and allowing it to propagate until all the intensity is in the adjacent guide. This calculation is shown in figure 8 for the same conditions given above.

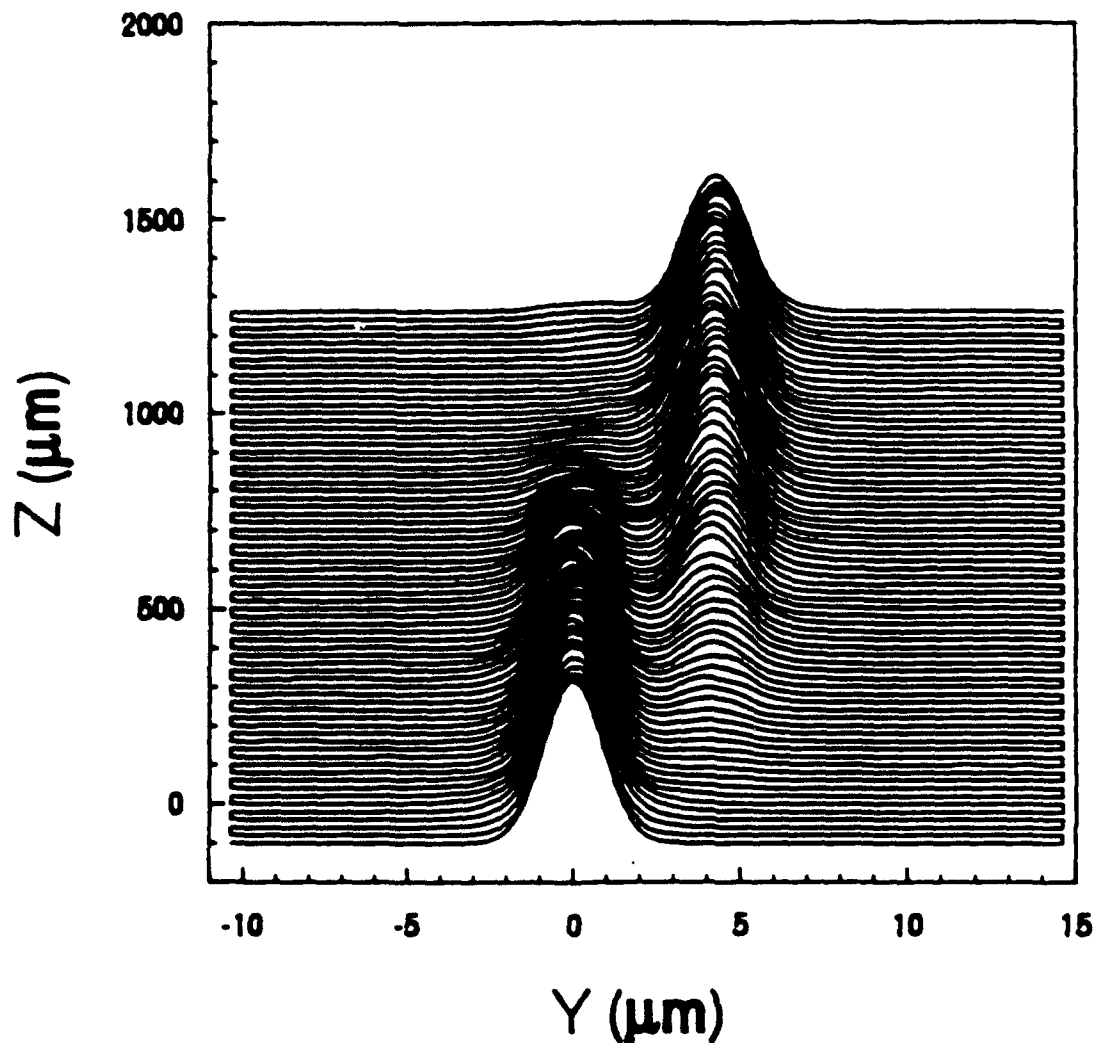


Figure 8. Output from the 2D beam propagator program for a pair of symmetric parallel waveguides with: widths=2.5mm, separation=1.75mm, cladding index= 3.4, waveguide index 3.4017. The coupling between the guides begins at $z=0$ and the intensity in the left guide reaches a minimum at $z=1.1\text{mm}$.

The agreement between the two calculations is good, though the beam propagator predicts a 10% longer coupling length. The beam propagator calculation is sensitive to the initial shape of the mode, which can change the result. In this case, the initial Gaussian distribution at $z = -100\mu\text{m}$ was allowed to propagate for $100\mu\text{m}$ before reaching the beginning of the right guide at $z=0$. This allows the mode to adjust to the guide before coupling affects the mode. Edge effects can also affect the results of the beam propagator calculation. In this case the calculation was made over a region $25\mu\text{m}$ wide so that the mode intensity was always zero at the edges.

4. Optical Properties of Quantum Wells

The electrooptic properties of the switches made in this program arise from the quantum wells in the cores of the planar waveguides used to fabricate the switches. In this program, waveguides containing both coupled and uncoupled quantum wells were fabricated.

4.1. Uncoupled Quantum Wells

The material used in all the switches made in this program is composed of GaAs and $\text{Al}_x\text{Ga}_{1-x}\text{As}$ grown using molecular beam epitaxy. By growing thin layers of GaAs surrounded by $\text{Al}_x\text{Ga}_{1-x}\text{As}$ quantum wells are formed that exhibit the now well known quantum confined Stark effect (QCSE). This can be used to create an optical absorption in the core of a waveguide that shifts to longer wavelength (red shifts) when a field is applied across the quantum well containing layer.⁸

4.2. Coupled Quantum Wells

In an earlier program, a new quantum well structure was developed at Martin Marietta Laboratories. This structure consists of two quantum wells of different width separated by a thin barrier. We call this structure an asymmetric coupled quantum well (ACQW). If the barrier between the wells is sufficiently narrow, the wavefunctions will have significant probability in both wells so that transitions between the levels in the two wells are possible. Figure 9 is a band diagram of the ACQW structure shown at three field values. For clarity, only the lowest energy hole state (the heavy hole of the wide well), and the two lowest energy conduction band states are shown in the diagram. For an optical modulator, the lowest energy transition is the most important since it determines the absorption edge of the long-pass filter formed by the quantum wells. At zero field (Fig. 9a) the lowest energy transition corresponds to the spatially direct transition within the wide well. The next highest transition at zero field is the spatially indirect transition from the wide well to the narrow well. As a field is applied, the conduction band levels approach each other. When these two

levels reach their minimum separation, the system is in resonance as shown in Fig. 9b. At resonance there is no distinction between the narrow and wide well conduction band states, and the two transitions have the same strength. At higher fields (Fig. 9c), the wavefunctions again become localized in individual wells. The lowest energy transition is now the indirect transition from the wide well to the narrow well. Because of the spacing between the wells, this transition energy drops rapidly as the field is increased. Although the strength of the transition also drops with applied field, it is strong enough to cause nearly complete extinction in a waveguide even at high fields. The inset in Fig. 9 shows a plot of the transition energies vs. field for the structure. Also shown are the transition energy of a single well and a horizontal line representing the energy of optical radiation passing through the waveguide. At zero field (a), both transitions are above $h\nu$ so there is no absorption. Beyond resonance (b), the energy of the indirect transition drops rapidly below $h\nu$ resulting in absorption in the waveguide. Beyond resonance (c) the direct transition (which corresponds to the single wide well transition) also eventually drops below $h\nu$ but only at higher field.

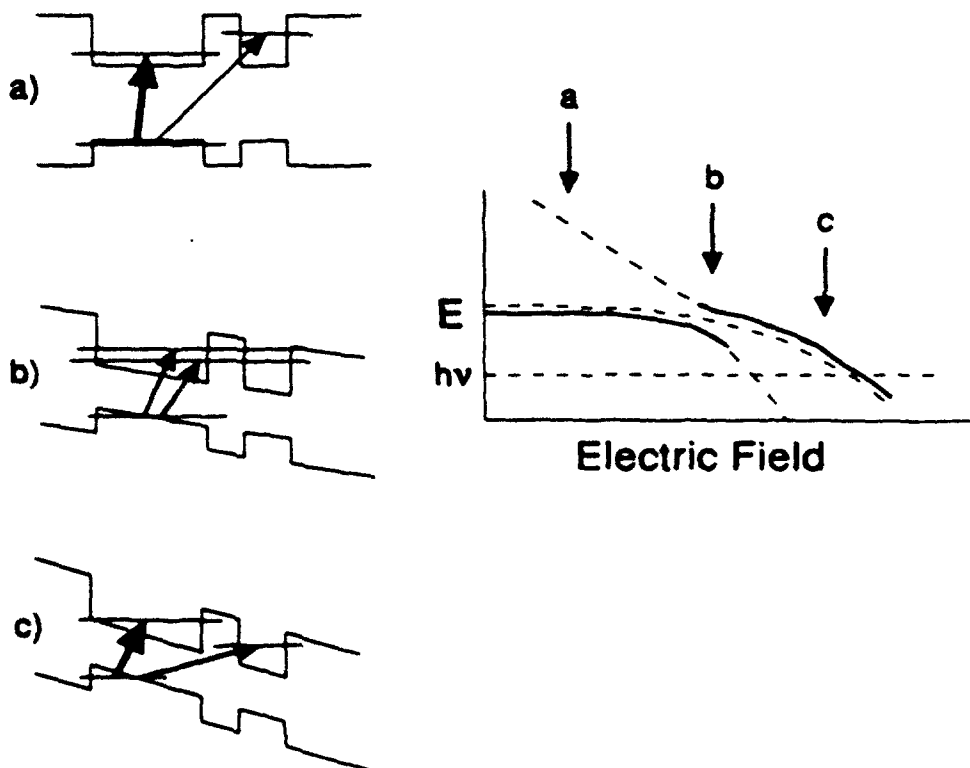


Figure 9. Effect of an externally applied electric field on the ACQW structure.

Figure 10 shows the measured bias dependent photocurrent spectra of a p-i-n diode containing an ACQW. At 5V, the weak indirect transition (h_1-e_1) becomes visible and moves rapidly toward longer wavelength as the bias is increased. The weak indirect transition in a waveguide would lead to nearly complete extinction of the optical mode, as shown in Fig. 11.

Figure 11 shows measured transmission through two waveguides (500 μ m long) containing a single quantum well (SQW) structure in one guide and an ACQW in the other. The indirect transition in the ACQW reduces the transmission of the guide to zero at about 11V. The SQW guide does not reach zero transmission until about 15V. Also shown in Fig. 11 are measurements of the phase shifts caused by biasing the two guides. Since the applied bias causes changes to the absorption spectrum in the waveguide, the refractive index must also change according to the Kramers Kronig relations. The indirect transition in the ACQW waveguide causes a 60% increase in the phase shift

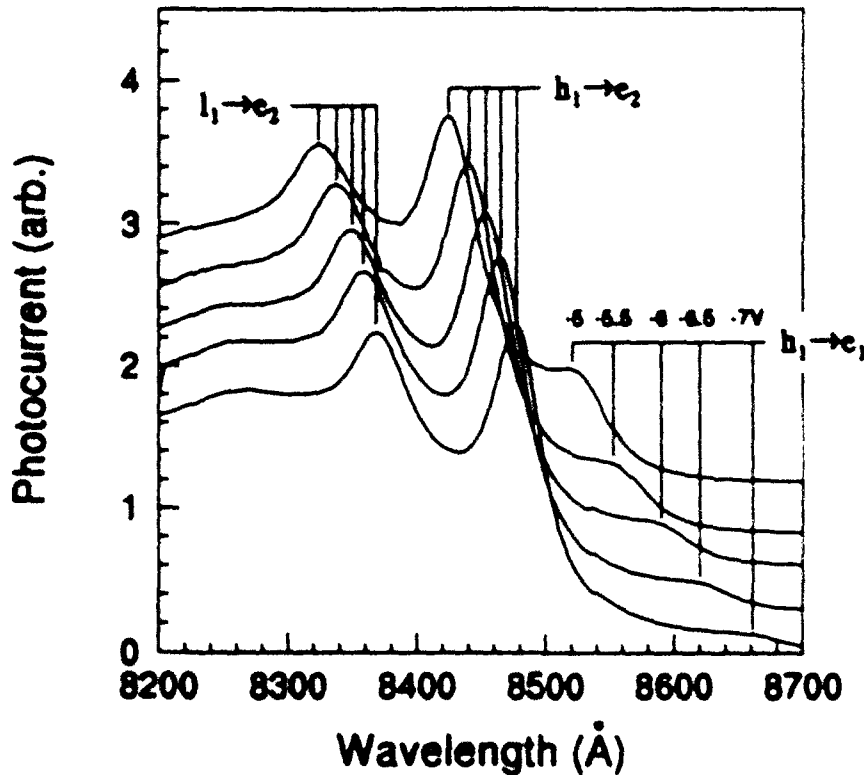


Figure 10. Photocurrent spectra of an ACQW structure at 5 values of applied bias. The $h_1 \rightarrow e_1$ peaks are caused by the spatially indirect transition from the wide well to the narrow well.

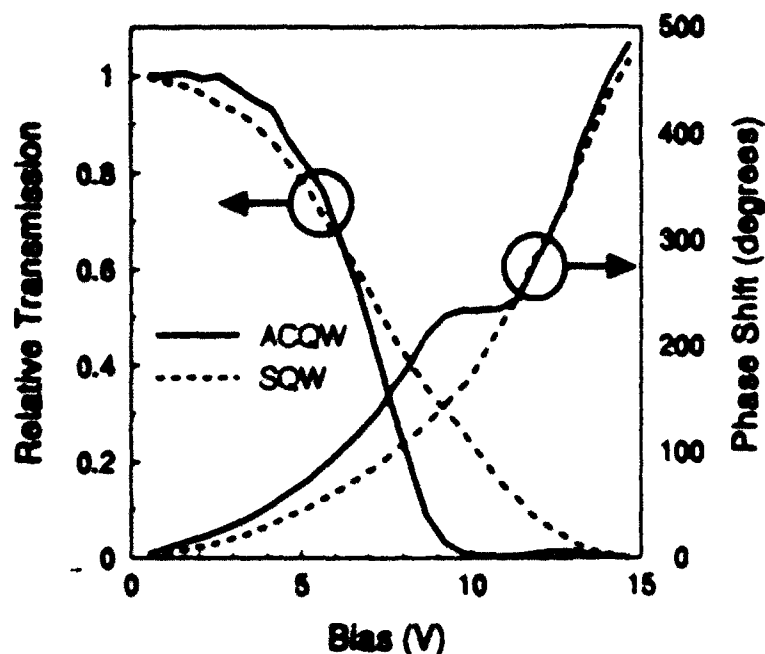


Figure 11. Comparison of transmission and phase shift measurements for two waveguides containing ACQW and SQW structures.

before it passes through the laser wavelength and the two phase shift curves converge to the same value.

5. Fabrication of Waveguide Structures

As described in sections 2 and 3, the waveguides are formed by etching the MBE-grown planar waveguide. This produces an effectively higher index under the unetched regions compared to the etched regions. In this program, two methods were used to fabricate the waveguides. The first, which we will call photoresist masking (PR masking), was used only on the early coupled waveguide structures. This method was replaced with a much simpler process that produced much more accurate waveguide dimensions and allowed narrower guides to be fabricated. We will refer to this improved process as the metal masking process.

5.1. Photoresist Masking Process

In this process, the waveguides are first defined by a photoresist pattern that is used as an etch mask to form the waveguides. This is followed by an RIE to etch the areas not masked by the PR, thus producing the waveguide ridges. In the structures made by this method the etch depth was $0.8\mu\text{m}$, producing

waveguide ridges $0.8\mu\text{m}$ high. (The upper cladding thickness was $1.5\mu\text{m}$ in these structures.) After etching, a metal strip was applied down the center of the waveguides to form the electrical p-contact. The whole structure was then covered with polyimide and openings were made over the p-contact strips. Finally, another layer of metal was added to form leads from the p-contacts to the bonding pads that were also formed by this final metal layer.

This process has several critical steps that made it difficult to accurately reproduce. The two most critical steps are the alignment of the p-contacts to the waveguides and the alignment of the openings in the polyimide to expose the p-contacts. In both cases, a narrow strip ($3\mu\text{m}$ wide in this case) had to be aligned to the narrow ($5\mu\text{m}$ wide) waveguide. Although this can be accomplished in structures this wide, the more advanced structures require narrower waveguides, which would make this process impractical.

Waveguides produced by this process were used for the 3mm evanescently coupled waveguide switch described in section 6.1.

5.2. Metal Mask Process

Because of the difficulties in the PR-mask process and because calculations showed that shorter switches required even narrower waveguides, we developed a new process for the waveguide fabrication. In this process (the metal mask process), the waveguide structure is first defined by applying a metal pattern to the surface of the wafer. This metal pattern is used as the etch mask to form the waveguides and also forms the p-contact on the top of the waveguides. As in the previous method, a reactive ion etch is used to form the waveguide. The advantage of this method is that the metal contact is "self-aligned" to the waveguide so that no critical alignment is required to apply the contact. In order for separate waveguides to be electrically isolated from one another, the planar waveguide is grown with the p-doped cap thinner than the etch used to define the waveguides. In this way the top conducting layer is completely removed outside of the waveguides ridges so that the areas between the waveguides are semi-insulating. The resulting waveguides are electrically isolated from each other. Measurements of the resistance between pairs of waveguides, $500\mu\text{m}$ long and separated by $1.1\mu\text{m}$, were greater than $30\text{M}\Omega$, which can be considered completely isolated for the structures presented here.

One possible disadvantage to this structure is that since the metal defines the waveguide, the only way to electrically isolate sections of the same waveguide is to leave gaps in the metal pattern, which also leaves gaps in the waveguide. This is not a problem as long as the waveguides are weakly

guiding. For the material used in this program, the effective index under the etched waveguides is only 0.1% greater than the effective index in the surrounding etched areas. This means that the reflection coefficient at an abrupt end of a waveguide will be only about 0.02% which is negligible. In addition to the reflection losses there is also some diffraction loss to the spreading of the unguided light in the gap. This also causes only a small loss as calculated using the beam propagator described in section 3.2.

For more complex structures, electrical connections to the waveguide structures can require electrical conductors that cross waveguides without connecting to them. This can also be easily accommodated with this structure. To form an electrical conductor crossing a waveguide, a 4- μm gap is left in the waveguide and a 2- μm -wide conducting strip crosses through the gap perpendicular to the waveguide. The metal of the electrical conductor is put down at the same time as the p-contact waveguide metal. This means that the electrical conductor is also etched with the waveguide and so forms a ridge in the final structure. Even though the electrical conductor is structurally the same as the waveguides, no light couples into it because it is normal (or nearly so) to the waveguides. At each electrical lead crossing, there will be a gap in the waveguide and the ridge formed by the lead. Because the effective index change under the lead is the same as that under the waveguide (which is very small as described above), it will also produce only a small reflection.

To measure the effect of both waveguide gaps for electrical isolation and gaps with crossing electrical conductors, we fabricated waveguides 1100 μm long with 4- μm -long gaps spaced every 100 μm along the waveguide. In one set of these, the gap was left empty, in another set each gap had a 2- μm -wide ridge crossing the gap perpendicular to the waveguide. Along side these waveguides was a similar waveguides with no gaps that was used for comparison. The configuration for these guides is shown in Fig. 12. The worst case measurement for the transmission through the two test guides relative to the reference guide was $T=65\%$ for both test guides. This corresponds to a transmission through a single gap of 95.7%. This is not a significant loss as long as the number of such gaps is kept to a reasonable level for any given waveguide.

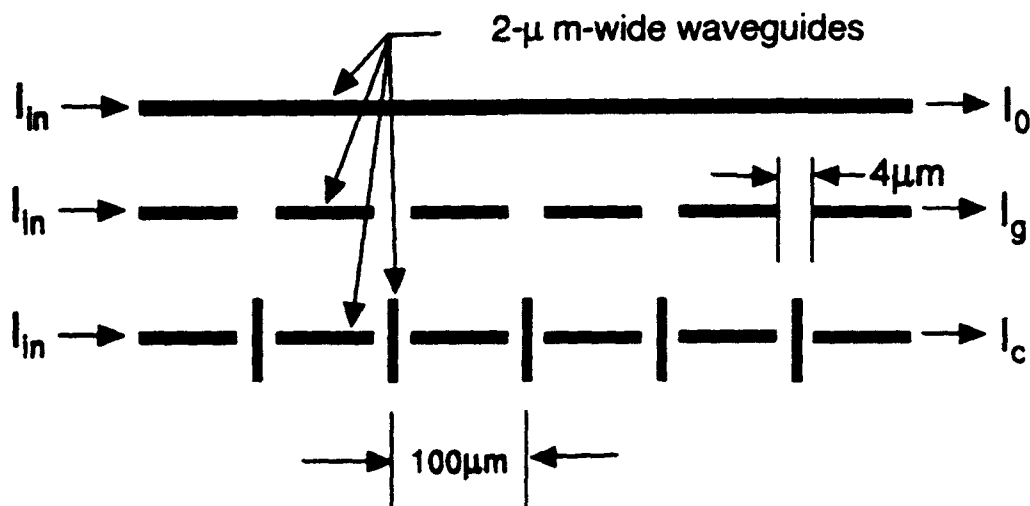


Figure 12. Waveguide structures used to determine the loss caused by gaps in the waveguides used for electrical isolation.

6. Coupled Waveguide Switch ($\Delta\beta$ Switch)

The first type of switch fabricated and tested in this program was a $\Delta\beta$ switch consisting of two 5- μm -wide waveguides separated by 2.5 μm . In this type of switch, the waveguides are designed so that at zero bias light entering one guide (the feed guide) will be completely transferred to the adjacent guide (the cross guide) in the length of the switch. This transfer requires that the two waveguides be identical. Switching is achieved by applying a bias to one of the waveguides. This changes the propagation constant (β) of the guide via the QCSE of the quantum wells in the guiding layer. This increases $\Delta\beta$ between the two guides so that the transferred intensity couples back to the original guide. The increase in $\Delta\beta$ between the two guides also tends to uncouple them so that less light is transferred.

6.1. Theory of the $\Delta\beta$ Switch

The $\Delta\beta$ switch can be analyzed both numerically and analytically, though the analytical description contains parameters that can only be determined using the full numerical analysis. In spite of this, the analytical analysis can provide insights to the effect of variations in the structure. For this reason, we will first describe the analytical analysis of the switch followed by an analytical tolerance analysis of the switch. The analytical analysis will be followed by the

conceptually simpler numerical analysis, which will be used to calculate parameters for fabrication of the $\Delta\beta$ switches.

6.1.1. Analytical Analysis of the $\Delta\beta$ Switch

A simple analysis of the $\Delta\beta$ switch can be made using the expressions given by Somekh et al.⁹ for a waveguide directional coupler. The expressions for the intensities in the guides are given in Eq. E6.1.1-1. In practice, The coupling constant K is determined using the numerical coupled waveguide calculation.

$$P_0(z) = \cos^2(S \cdot z) + \left[\left(\frac{\Delta\beta_{\text{bias}}}{2} \right)^2 / S^2 \right] \cdot \sin^2(S \cdot z) \quad (\text{E6.1.1-1})$$

$$P_1(z) = \frac{K^2}{S^2} \cdot \sin^2(S \cdot z)$$

where:
$$S = \sqrt{K^2 + \left(\Delta\beta_{\text{bias}} / 2 \right)^2}$$

$\Delta\beta_{\text{bias}}$ = the change in the propagation constant
in the biased guide due to the applied bias

The cross-over length, L_x , is defined as the length required for all the radiation to cross from the input guide to the cross guide. The relation between L_x and the coupling constant is given in Eq. E6.1.1-2.

$$K = \frac{\pi}{2 \cdot L_x} \quad (\text{E6.1.1-2})$$

To switch to the bar state, the propagation constant of one of the guides must be changed by $\Delta\beta$ according to the conditions given in Eq. E6.1.1-3.

$$S = \pi / 2 \cdot L_x \quad (\text{E6.1.1-3})$$

$$\Delta\beta = \frac{\pi \cdot \sqrt{3}}{L_x} = 2\sqrt{3} \cdot K$$

Substituting $\Delta\beta$ into the intensity expressions (Eq. 6.1.1-1) yields the expressions (Eq. 6.1.1-4) for the intensities in the two guides of a lossless $\Delta\beta$ switch.

$$P_0(z) = \cos^2\left(\frac{\pi}{L_x} \cdot z\right) + \frac{3}{4} \cdot \sin^2\left(\frac{\pi}{L_x} \cdot z\right) \quad (\text{E6.1.1-4})$$

$$P_1(z) = \frac{1}{4} \cdot \sin^2\left(\frac{\pi}{L_x} \cdot z\right)$$

The absorption in each guide can be estimated by weighting the electrically induced absorption coefficient in each guide (α_{bias}) by the intensity in that guide and integrating along the length of the guide as shown in Eq. E6.1.1-5.

$$\alpha_i \approx \int_0^{L_x} P_i(z) \cdot \alpha_{\text{bias}} dz \quad (\text{E6.1.1-5})$$

Integrating the expressions in Eq. E6.1.1-4 yields the results given in Eq. E6.1.1-6.

$$\alpha_{\text{branch}} \approx \frac{1}{8} \cdot \alpha_{\text{bias}} \quad (\text{E6.1.1-6})$$

$$\alpha_{\text{feed}} \approx \frac{7}{8} \cdot \alpha_{\text{bias}}$$

This result shows that the absorption coefficient in the biased guide is about seven times that of the unbiased guide. This has an important effect on the switching properties of the $\Delta\beta$ switches as demonstrated below.

6.2. Tolerance Analysis

An important consideration in the fabrication of the switches is the effects of errors in the switch dimensions. All fabrication in this program was done using standard contact lithography techniques. We found the most important variation in the fabrication was in the width of the waveguides. During the fabrication process, changes in the exposure of the pattern using the ultraviolet lamp in the aligner, or changes in the development time can change the width of the resulting waveguides. This change in width is equal for all the waveguides on a wafer so the resulting switch is still symmetric, but may have a slightly different crossover length than desired. Since the length of the switch is fixed by design, this can lead to incomplete cross-over resulting in crosstalk.

The effects of these width variations can be determined by calculating their effects on the coupling length. Using Eq. 6.1.1-1 the cross-talk can be determined and is given in Eq. 6.2-1.

$$R_x = \left(\frac{\pi \cdot \delta}{2 \cdot L_x} \right)^2 \quad (\text{E6.2-1})$$

where:

$$R_x = \frac{\text{intensity out of the feed guide}}{\text{intensity out of the branch guide}}$$

$$\delta = \text{error in the cross over length } (L_x)$$

For an ideal switch, R_x would be zero. For a switch with an isolation of 100:1 ($R_x < 0.01$), the error in the coupling length must be less than 6%.

To determine how L_x varies with the waveguide width, a numerical calculation is used to calculate both L_x and dL_x/dW . This calculation is described in the next section, and some example values of L_x and dL_x/dW are given in Table I. Once these parameters are determined, δ in E6.2-1 can be replaced with

$$\delta = \frac{dL_x}{dw} \cdot \Delta w$$

where Δw is the error in the waveguide widths. The resulting condition on the waveguide widths is given in E6.2-2.

$$\Delta w \leq \frac{2 \cdot L_x \cdot R_x^{1/2}}{\pi \cdot \frac{dL_x}{dw}} \quad (\text{E6.2-2})$$

For a 100:1 isolation ($R_x = 0.01$) the maximum allowable errors for the two $\Delta\beta$ switches produced are:

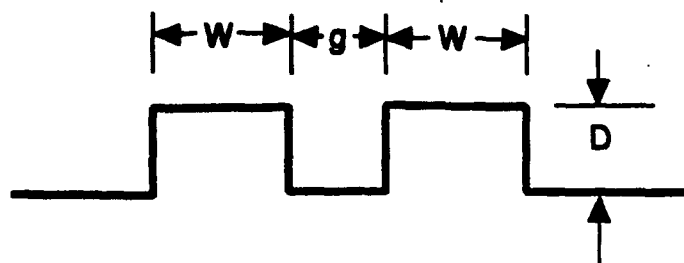
3.0mm switch	$\Delta w < 0.64\mu\text{m}$
0.5mm switch	$\Delta w < 0.29\mu\text{m}$

These values are greater than 10% of the waveguide width. This level of accuracy is easily achieved using the metal mask process described in sec. 5.2.

6.2.1. Numerical Analysis of the $\Delta\beta$ Switch

To calculate the optical modes and cross-over length of the $\Delta\beta$ switch, the planar waveguide calculation (described in sec. 3.1) is used. The first step in the process is to calculate the effective index of the planar waveguide structure as the top cladding layer is numerically "etched" away. Once this is accomplished, the modes of the coupled waveguides can be calculated. For the modal calculation, the two waveguides and cladding are treated as a five layer planar waveguide with the refractive index of the layers 1/2/3/4/5 set to the effective index values of cladding/ridge/cladding/ridge/cladding. The symmetric and anti-symmetric modes of this five layer structure are calculated. This produces the values of the propagation constants β_1 and β_2 . From their difference, the coupling constant can be determined ($K=\beta_1-\beta_2$), which gives the cross-over length ($L_X=\pi/2K$). The program written to perform this calculation produces tables of L_X and dL_X/dw as a function of rib height (etch depth) and rib separation. By repeating the calculation for various rib widths, a complete set of tables for fabricating switches of various lengths can be produced. A subset of the results of these calculations is given in table I. It should be noted that the rib height given in the table is dependent on the underlying planar waveguide structure. For this reason, the more generally applicable values of dn/n are given (where n =index of the etched areas and $n+dn$ = the index under the ridges), the value of n for these structures is approximately 3.5.

Table I. Calculated dimensions for evanescently coupled waveguides. The parameters are chosen so that $dL_x/dn=0$ to minimize the effects of fabrication errors.



$L_x(\text{mm})$	$W(\mu\text{m})$	$g(\mu\text{m})$	dn/n	$D(\mu\text{m})$	$dL_x/dW (\text{mm}/\mu\text{m})$
3.0	5.00	2.50	1.7×10^{-4}	0.36	-0.30
2.0	4.00	2.25	2.4×10^{-4}	0.44	-0.21
1.5	2.75	2.50	3.6×10^{-4}	0.49	-0.14
1.0	2.50	1.75	5.0×10^{-4}	0.52	-0.14
0.5	2.00	1.10	1.0×10^{-3}	0.62	-0.11

6.3. 3-mm Long $\Delta\beta$ Switch

The first $\Delta\beta$ switch was designed to have a crossover length of 3mm. The parameters for this switch are shown in Table I. A cross-section of the waveguide structure is shown in Fig. 13. The waveguides are $5\mu\text{m}$ wide with a $2.5\text{-}\mu\text{m}$ gap between them. Because these first switches were made on an early planar waveguide structure, which has a thick upper cladding layer, the etch depth to form the ribs was $0.8\mu\text{m}$ (not $0.36\mu\text{m}$ as shown in the table). These waveguides were made by first etching the ribs, then planarizing the structure with polyimide and finally applying the top metal connections.

The measured near-field intensity at several bias voltages is shown in Fig. 14. The coupling in this switch is incomplete, which causes the 0V curve to

have a large right peak (input was on the left side) as expected, but with the addition of a shoulder on the left which would not be present if the coupling was correct. Previous measurements made before application of the electrical contacts and polyimide showed that the coupling between the two guides should have been nearly complete, indicating that the coupling problems arose during the application of these features. Several problems became apparent during the further fabrication of this switch and the 500- μm -long switch described in the next section. These were: 1) The polyimide pulled away from the switch changing the coupling conditions as a function of position down the waveguide, 2) variations in the photolithography changed the width and spacing between the waveguides, which also changed the coupling conditions as a function of length, and 3) errors in the growth rates during the MBE growth of the planar waveguide structure caused errors in the coupling. Several steps were taken to eliminate these problems.

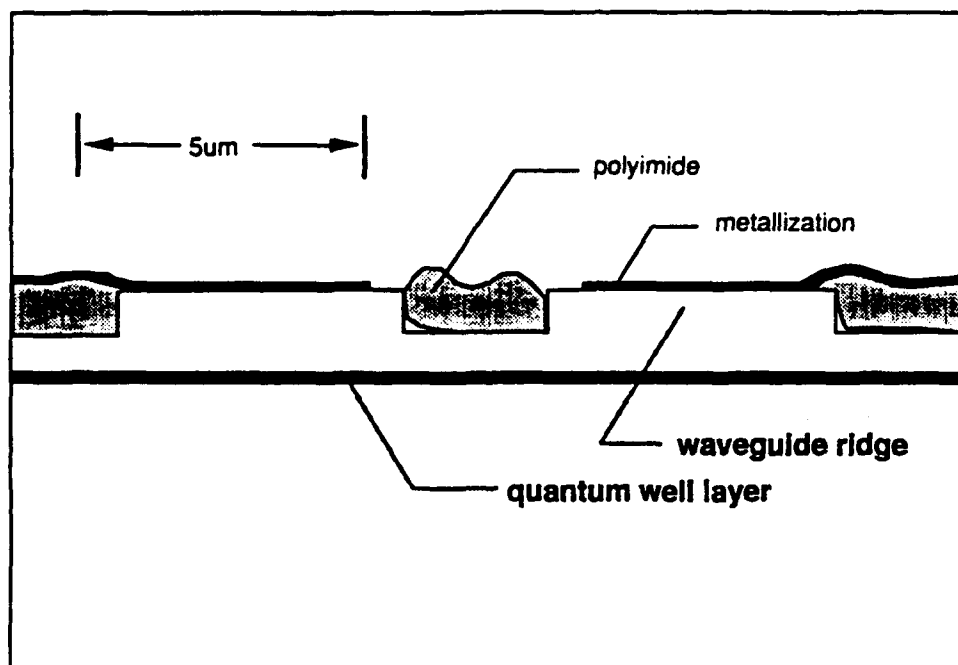
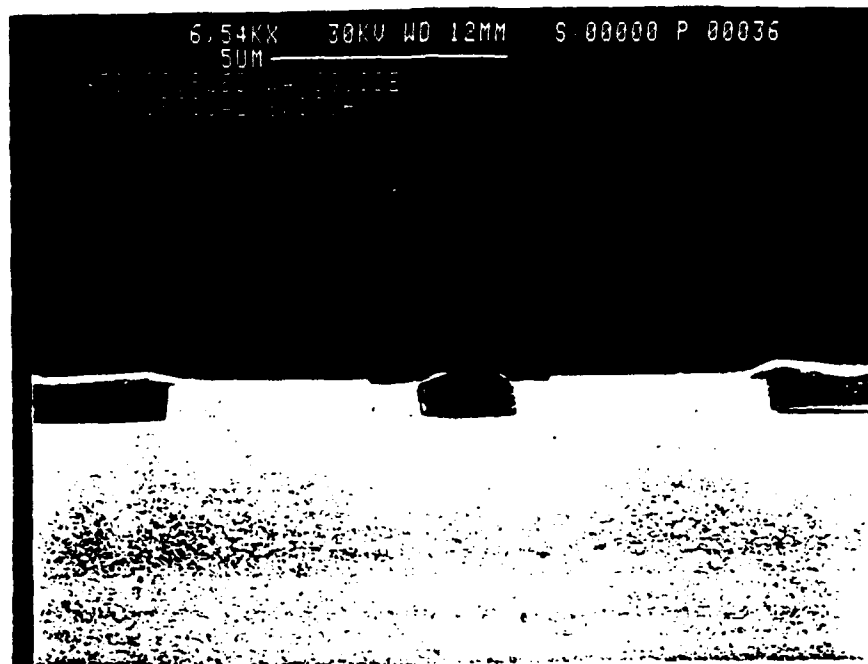


Figure 13. SEM micrograph of the 3-mm-long $\Delta\beta$ switch cross-section (top) and a diagram identifying the parts of the structure (bottom).

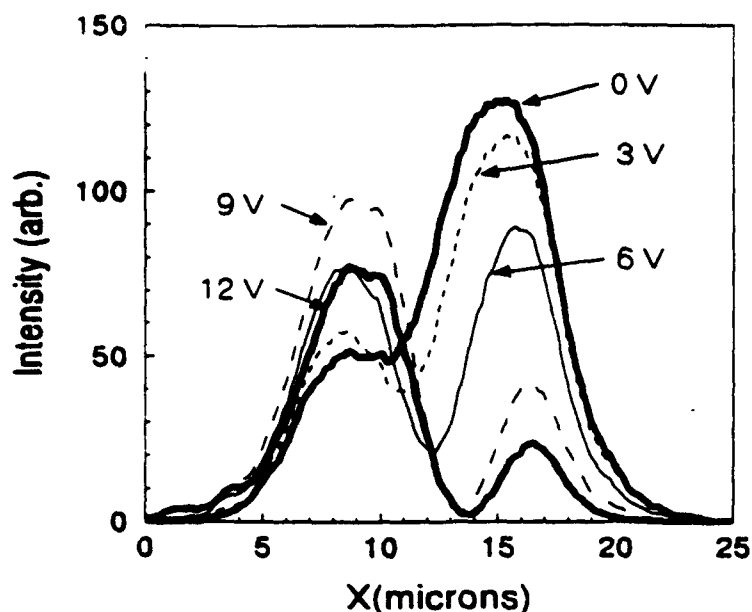


Figure 14. Near-field output of the $\Delta\beta$ switch as a function applied bias.

To detect problems with the layer thicknesses in the MBE grown planar waveguides, superlattices with a period of 100Å were used for the waveguide cladding. Superlattice cladding had already been used on many of the planar waveguides to prevent dopants from migrating out of the doped layers during growth. By including a superlattice near the top of the structure, it is possible to use x-ray diffraction to determine the actual period and detect errors in the growth rate. Figure 15 shows an x-ray diffraction measurement of one of these structures (in this case the SL period was designed to be 60Å). The small peak at 67.77° is the SL diffraction peak, which corresponds to an actual SL period of 59.8Å (the design value for this structure was 60Å). (The large peak at 66.4° is not a diffraction feature, but is caused by turning up the x-ray power at that point in the scan so that the weak SL peak is visible.)

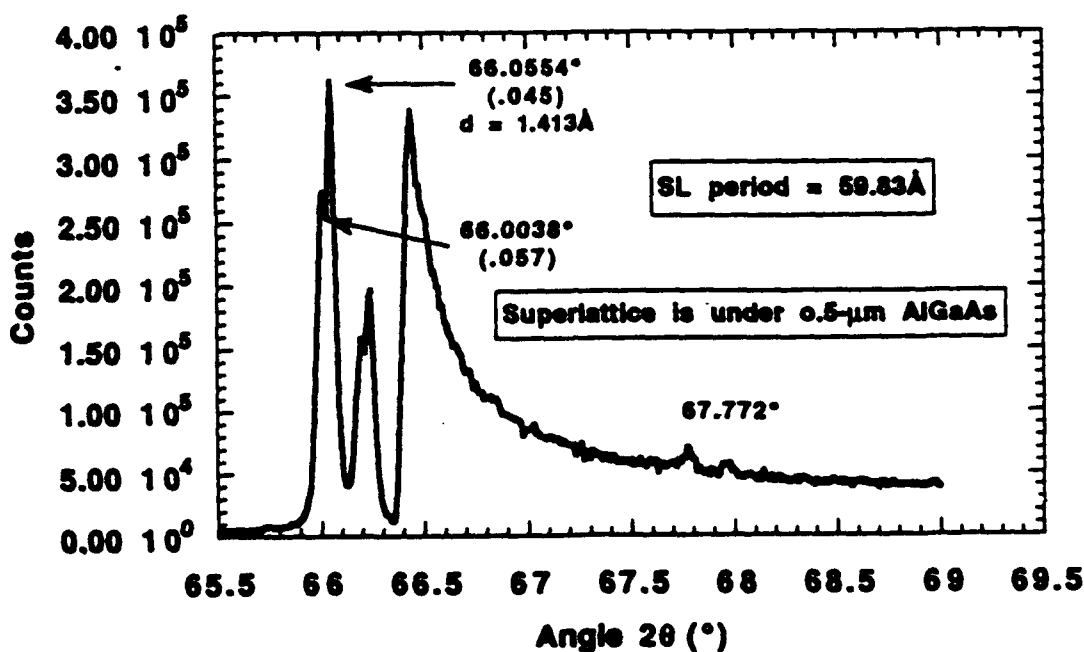


Figure 15. X-ray diffraction spectrum of a waveguide structure with SL cladding

To reduce processing problems and lower the switching voltage, changes were made to the planar waveguide layer thicknesses. In the new design, the intrinsic region was made thinner ($1.275\mu\text{m}$ instead of $1.64\mu\text{m}$) while the core width was increased to increase the confinement. This reduced the ridge etch required for the switches from $0.75\mu\text{m}$ to $0.40\mu\text{m}$, which simplified the processing. The thinner intrinsic region also lowered the switching voltage. The form of the two structures is shown in Fig. 16.

cap	$p^+ 2 \times 10^{18}$	500Å GaAs	
doped cladding	$p^+ 2 \times 10^{18}$	$\left\{ \begin{array}{l} 85\text{\AA} \text{ Al}_x\text{Ga}_{1-x}\text{As} \\ 15\text{\AA} \text{ GaAs} \end{array} \right\} \times 45$	
intrinsic cladding	SL	$\left\{ \begin{array}{l} 85\text{\AA} \text{ Al}_x\text{Ga}_{1-x}\text{As} \\ 15\text{\AA} \text{ GaAs} \end{array} \right\} \times 105$	
MQW layer		$\left\{ \begin{array}{l} 100\text{\AA} \text{ Al}_x\text{Ga}_{1-x}\text{As} \\ 100\text{\AA} \text{ GaAs} \\ 25\text{\AA} \text{ Al}_x\text{Ga}_{1-x}\text{As} \\ 50\text{\AA} \text{ GaAs} \end{array} \right\} \times 7$	
intrinsic cladding	SL	$\left\{ \begin{array}{l} 85\text{\AA} \text{ Al}_x\text{Ga}_{1-x}\text{As} \\ 15\text{\AA} \text{ GaAs} \end{array} \right\} \times 40$	
doped cladding	$n^+ 2 \times 10^{18}$	$\left\{ \begin{array}{l} 85\text{\AA} \text{ Al}_x\text{Ga}_{1-x}\text{As} \\ 15\text{\AA} \text{ GaAs} \end{array} \right\} \times 135$	
buffer	$n^+ 2 \times 10^{18}$	5000Å GaAs	
n^+ GaAs substrate			

a) First $\Delta\beta$ epitaxial structure

Cap	$p^+ 2 \times 10^{18}$	500Å GaAs	
Doped cladding	$p^+ 2 \times 10^{18}$	2500Å $\text{Al}_x\text{Ga}_{1-x}\text{As}$	
Intrinsic cladding	SL	$\left\{ \begin{array}{l} 85\text{\AA} \text{ Al}_x\text{Ga}_{1-x}\text{As} \\ 15\text{\AA} \text{ GaAs} \end{array} \right\} \times 60$	
MQW layer (waveguide core)		$\left\{ \begin{array}{l} 100\text{\AA} \text{ Al}_x\text{Ga}_{1-x}\text{As} \\ 100\text{\AA} \text{ GaAs} \\ 25\text{\AA} \text{ Al}_x\text{Ga}_{1-x}\text{As} \\ 50\text{\AA} \text{ GaAs} \end{array} \right\} \times 10$	
Intrinsic cladding	SL	$\left\{ \begin{array}{l} 85\text{\AA} \text{ Al}_x\text{Ga}_{1-x}\text{As} \\ 15\text{\AA} \text{ GaAs} \end{array} \right\} \times 40$	
Doped cladding	$n^+ 2 \times 10^{18}$	$\left\{ \begin{array}{l} 85\text{\AA} \text{ Al}_x\text{Ga}_{1-x}\text{As} \\ 15\text{\AA} \text{ GaAs} \end{array} \right\} \times 110$	
Buffer	$n^+ 2 \times 10^{18}$	5000Å GaAs	
n^+ GaAs substrate			

b) Improved epitaxial waveguide

Figure 16. Epitaxially grown waveguide structures.

Measurements of a switch incorporating these improvements are shown in Fig. 17. At zero bias, the intensity peaks at the left guide (input is to the right guide) with a small residual intensity in the right guide. As bias is applied, the intensity decreases in the left guide and increases in the right guide. At 8V bias, the output of the right guide peaks at about 68% of the initial zero bias peak in the left guide. The peak intensity out of each guide as a function of bias is shown in Fig. 18. In Fig. 18a, the bias is applied to the branch guide. In this case the switched intensity from the feed guide at 8V bias is about 70% of the initial zero bias output from the branch guide (with a residual output from the branch guide about 10% of its initial intensity). In Fig. 18b, the feed guide is biased. In this case the output of the feed guide at the 8V switching potential is only about 17%

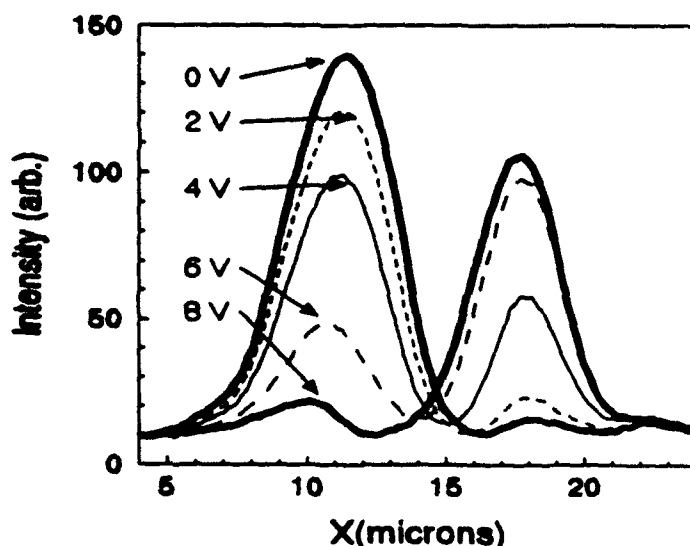


Figure 17. Near-field output of a 3-mm-long $\Delta\beta$ switch using the improved epitaxial structure.

of the initial cross guide output. This switching asymmetry is caused by the electroabsorption in the biased guide. When the feed guide is biased, optical losses are seven times higher than when the cross guide is biased, as described in section 6.1.1.

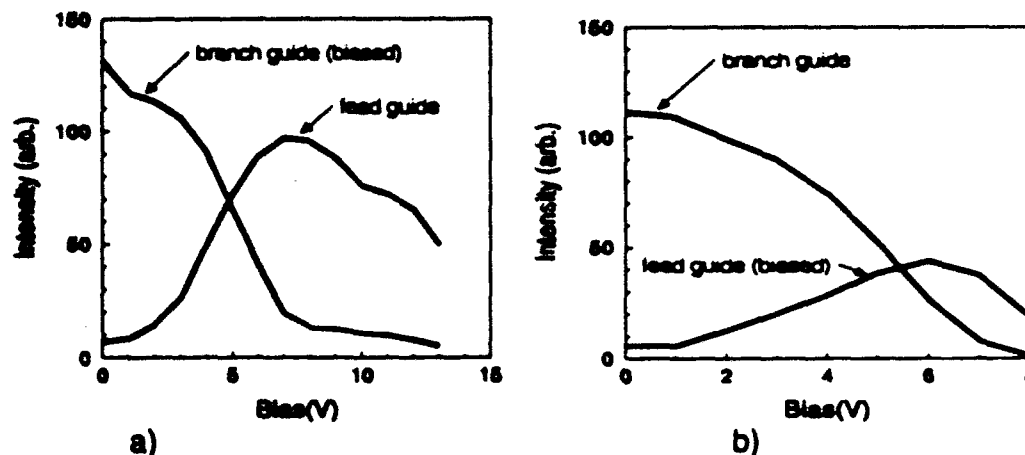


Figure 18. Intensity outputs from the $\Delta\beta$ switch for a) the branch guide biased and b) the feed guide biased.

Even with the inclusion of the superlattice in the thinner waveguide structure, this switch was still difficult to fabricate reliably. Coupling tests with guides having no electrical contacts usually showed much better results than the zero bias results in the two switches presented here. We found two problems remaining in this switch design. The first was the polyimide that was used to planarize the structure. By pulling away from the waveguide ribs, the polyimide created coupling conditions that changed along the length of the waveguides. The final problem was that we could not determine the precise composition (x -value) of the $\text{Al}_x\text{Ga}_{1-x}\text{As}$ in the planar waveguide structure. Both of these problems were solved in the 500 μm $\Delta\beta$ switch described in the next section.

6.4. 500- μm Long $\Delta\beta$ Switch

The second type of switch fabricated was a 500- μm -long $\Delta\beta$ switch. The dimensions of this switch are given in table I. The waveguides in this switch (and all subsequent waveguide structures made in this program) are 2 μm wide and etched to create an index difference between the guide and surrounding area of about 0.1%.

To correct problems with the photolithography accuracy and the polyimide, the processing and structure were changed from that of the 3-mm $\Delta\beta$

switch. The processing was changed to the metal mask process described in sec. 5.2. This process uses an image reversed photoresist that was found to produce the waveguide dimensions more accurately than the conventional positive photoresist process. In addition, the waveguides were defined by the top p-contact metal, which was then used as the mask for the RIE waveguide etch. This creates a waveguide with accurate width and with the contact metal already in place. This self aligned contact metal eliminates the requirement of aligning the contacts with the waveguide, which allows fabrication of narrow waveguides (required for a short $\Delta\beta$ switch) using standard contact lithography.

To allow determination of the material composition, a 0.5- μm -thick layer of $\text{Al}_x\text{Ga}_{1-x}\text{As}$ was included at the top of the structure over the SL. (This layer was covered with a 500Å GaAs cap to prevent oxidation of the AlGaAs.) This layer makes it possible to use photoluminescence (PL) to determine the composition of the $\text{Al}_x\text{Ga}_{1-x}\text{As}$ after growth. Since the same composition was used throughout the structure, this measurement gives the compositional accuracy of the structure.

With the addition of the superlattice cladding (described in the last section), the $\text{Al}_x\text{Ga}_{1-x}\text{As}$ top layer, and the self-aligned metal mask lithography process, the 500- μm $\Delta\beta$ switch could be reliably processed. These improvements were used in all subsequent waveguide structures produced in this program.

The structure of the 500- μm -long $\Delta\beta$ test switches is shown in Fig. 19. Each set of switches consists of five coupled pairs of 2- μm -wide waveguides with a 1.1- μm gap between them. Input to each pair is through a

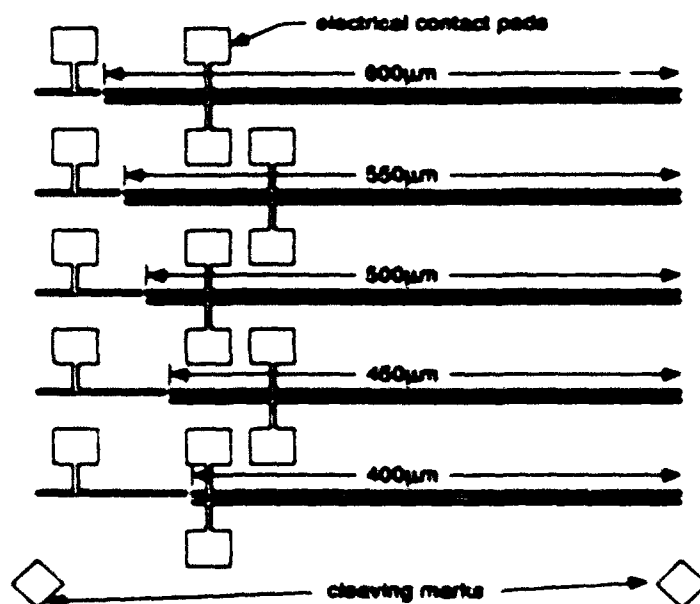


Figure 19. Test structure for the 500- μm -long $\Delta\beta$ switch.

single waveguide. The length of the coupled pairs is incremented by $50\mu\text{m}$ from pair to pair to allow for errors in the coupling length. The calculated coupling length as a function of the etch depth of the waveguides is shown in Fig. 20. We fabricate the waveguides so the switches operate at the minimum cross-over length. This not only gives the switch the shortest length for a given set of waveguide dimensions, but also makes the switch less susceptible to variations in the etch depth and waveguide widths. The near-field output of a $550\text{-}\mu\text{m}$ $\Delta\beta$ switch under several bias conditions is shown in Fig. 21.

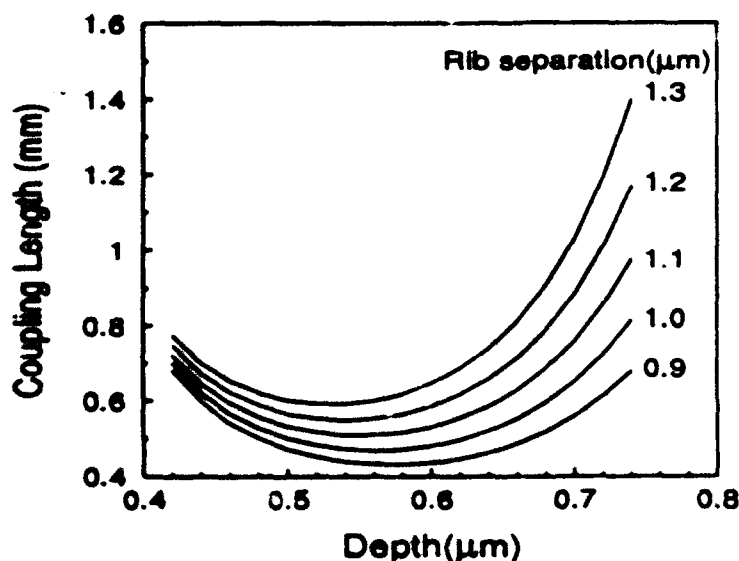


Figure 20. Calculation of coupling length vs. the rib etch depth. The etch depth was chosen to give the minimum coupling length for a given separation thus making the switch less sensitive to fabrication errors.

At zero bias, the output shows a well defined single peak that demonstrates complete coupling of the input light into the cross guide. As the bias is increased, a second peak appears at the output of the cross guide. At 15.5V volts the intensity in the bar guide reaches its peak value (about 85% of the initial cross guide output). A plot of the output intensities is shown in Fig. 22. This curve deviates from an ideal switch in that the switched output is 85% of the unswitched output instead of equal to it. This amount of loss could easily be corrected by adding gain at the output of the switch. A more serious problem with this switch is that it cannot be used with the input into the biased waveguide. In that case, applying bias to the switch causes strong absorption, which causes the output intensity to drop to near zero before the switching process is complete. This makes this $\Delta\beta$ switch suitable as

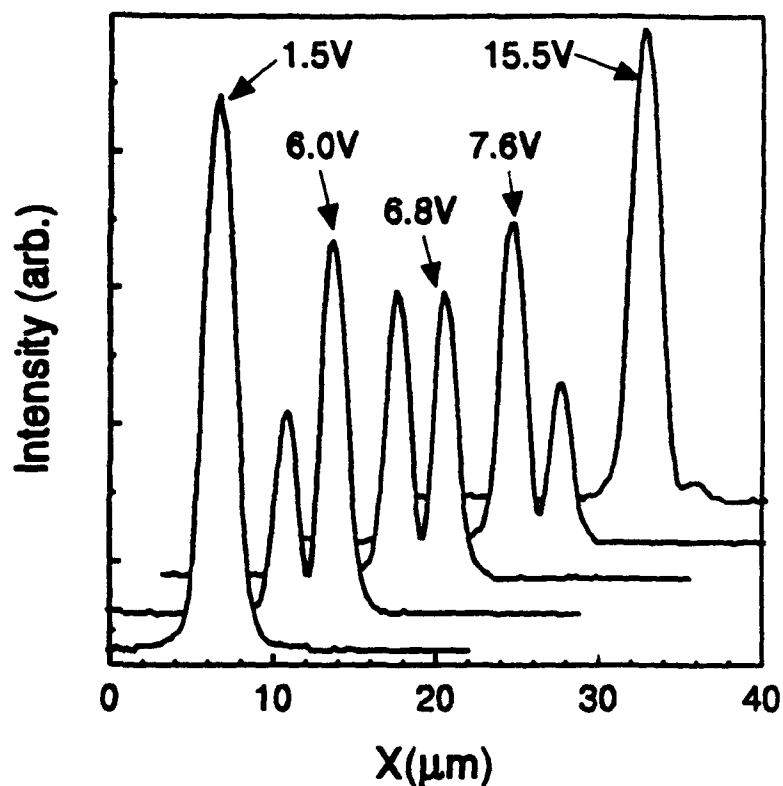


Figure 21. Near-field output of the 500-μm-long $\Delta\beta$ switch at 5 values of the applied bias.

a one-input two-output switch, but not as a 2x2 cross bar switch. This limitation was overcome in the $\Delta\alpha$ switch described in the next section.

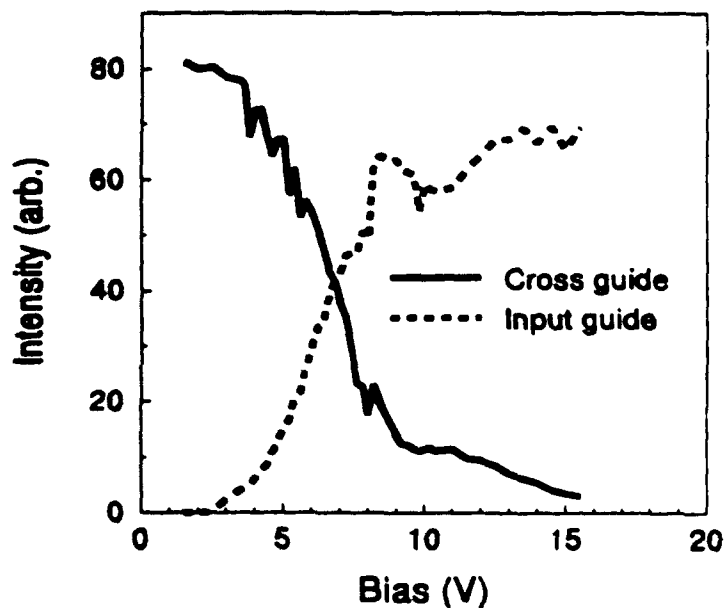


Figure 22. Output intensity from each guide as a function of applied bias.

7. The $\Delta\alpha$ Switch

The second type of switch developed in this program is called the $\Delta\alpha$ switch. The name comes from mode of operation, which uses the change in the absorption coefficient α caused by biasing the quantum wells to accomplish the switching. The general structure of this type of switch is shown in Fig. 23. It consists of four Y-splitters, two at the input end and two at the output end of the switch. In operation, light enters one the two input guides at the left of the structure. Each of these inputs is then split into two paths, which go to the two outputs at the right side of the switch. To switch to either a bar or cross state, the different paths can be reverse biased to make them absorbing. The bar state is formed by reverse biasing the cross in the center of the structure to make it opaque. In a similar way, the cross state is formed by reverse biasing the bar paths on each side of the switch to make them absorbing. The disadvantage to this type of switch is the splitting loss. Each time light passes through one of the Y-splitters (either entering from single or double waveguide side), its intensity is reduced by half. This means that at best 25% of the input will reach one of the outputs. To eliminate this loss, gain must be added to the structure. It would be possible to forward bias the entire structure so that all the waveguides would have gain. Switching could then be achieved by removing the bias or switching to reverse bias in those sections required to be opaque. There are two major disadvantages to that approach. First, the switch would require a great deal of electrical power, which would make cooling a problem in a large network. Second, switching gain on and off is a relatively slow process. For our approach, short gain sections at the inputs and outputs of the switch that are dc biased were chosen. Switching is achieved in the bar and cross paths by using waveguides that are transparent under zero bias and opaque under reverse bias. The reverse biased guides draw very little current and make high speed modulators so that high speed switching can be achieved.

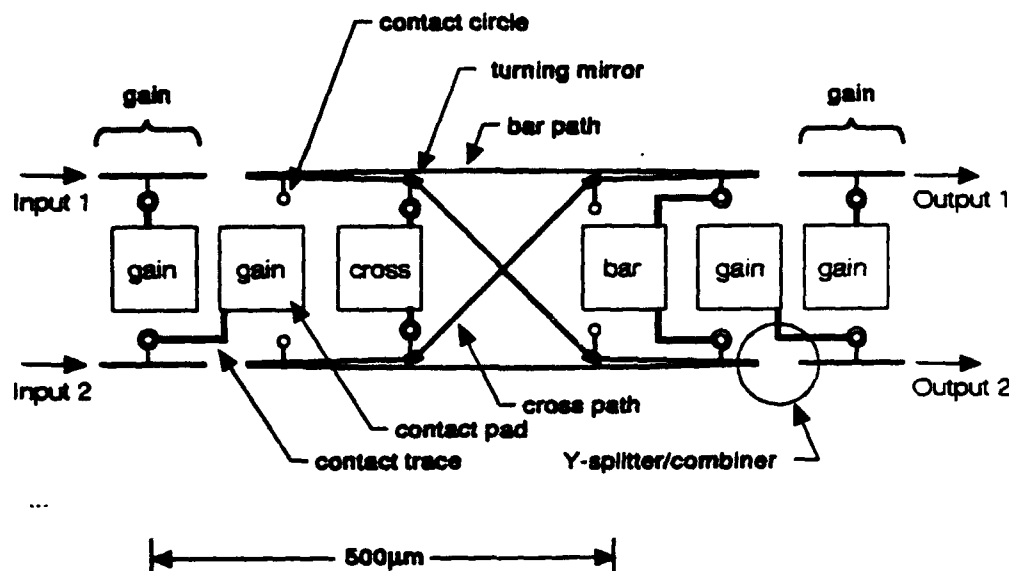


Figure 23. Design of the $\Delta\alpha$ switch.

The gain is produced, as in a laser, by forward biasing the junction containing the quantum wells. This gain, however, is at a wavelength that is strongly absorbed by the unbiased quantum wells. Since the entire switch structure is made on the same epitaxial structure, all the waveguides contain the same quantum wells. For the switch to operate, the QW exciton wavelength in the gain sections must be at a longer wavelength than the QW excitons in the rest of the structure. In the switch produced in this program, we accomplished this by using oxide induced disordering to blue shift the excitons in the modulator and transparent waveguide sections of the switch. This enabled us to achieve both gain and modulation at the same wavelength in the switch described below.

The switch is fabricated using the self-aligned metal mask process described in section 5.2. In this process, the waveguides are defined as a gold pattern on the surface of the wafer. This metal, which will form the p-contacts on top of the waveguides in the final structure, is used as the etch mask in the RIE process used to etch the waveguides. In addition to the waveguides, the contact circles (shown in fig. 23) as well as the connection between the contact circle and the waveguide (this is shown in greater detail in fig. 24) are put down in gold in this first step. Once the gold pattern has been defined, the structure is etched to form the waveguide ridges using RIE. After this step, a second etch is used to define the turning mirror facets (this is described in sec. 7.1.2). Finally, a thick gold pattern is applied forming the electrical contact pads. This final gold layer also includes the contact traces (shown in Fig. 23), that end in large circles that surround the contact circles described above. This overlap of the two circles in the two different layers, along with evaporation of the last metal layer at an angle

20 to 30° from normal, insures that electrical connection will be made between the two levels. An SEM micrograph of one of these circles is shown in Fig. 25. The electrical contact pads could be included in the waveguide layer, but this would make the pads themselves diodes, which would have several negative effects on the device. First, the chance that a diode will contain a defect (and thus be shorted and unusable) is proportional to the diodes area, so the area of each diode should be kept as small as possible. Second, a larger area diode has a larger capacitance (capacitance is proportional to the diode area) so for high speed applications the diode area should also be kept as small as possible. For high speed applications, it would be desirable to add a layer of a low dielectric constant insulator under the last metal layer. Either polyimide or SiO₂ could be used for this application resulting in a lower contact pad capacitance.

In the sections below, we describe the waveguide components of the switch followed by a description and demonstration of the first 2x2 $\Delta\alpha$ switch (which did not have gain). This is followed by a description of the oxide disordering process and results, and finally the test results on two 2x2 $\Delta\alpha$ switches with gain are presented.

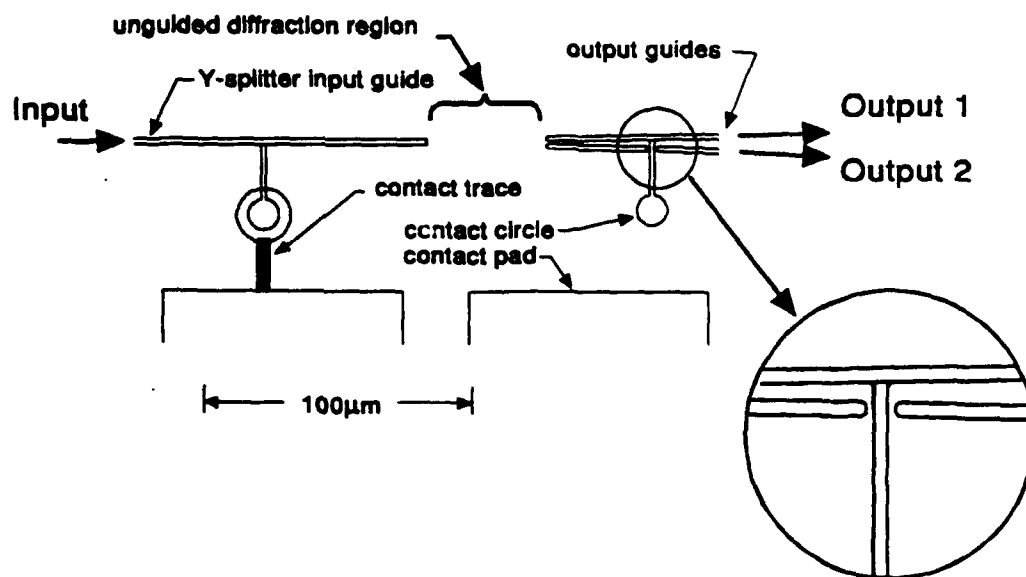


Figure 24. The Y-splitter structure used in the $\Delta\alpha$ switch. The inset shows the electrical trace going past the cross path to the bar path.

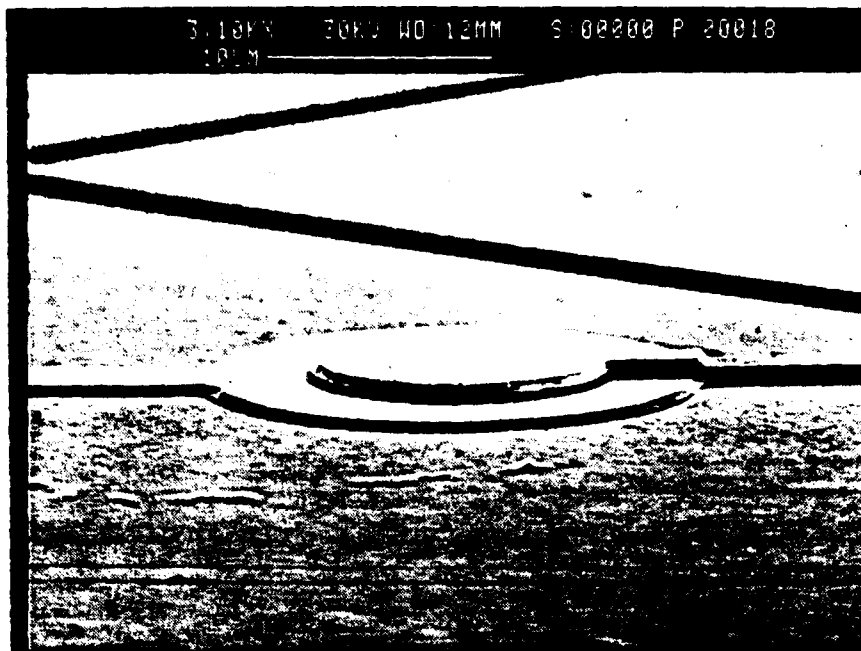


Figure 25. SEM micrograph of gold contact circles used to make electrical connections between the etched level and waveguide ridge level of the switch.

7.1. $\Delta\alpha$ Waveguide Switch Structures

The first of two designs of the $\Delta\alpha$ switch is shown in fig. 23. As already described, this switch operates by splitting each input into two paths so that each input can be routed to either of the two outputs. Light enters the switch at either of the two inputs shown at the left, and travels through a 100- μm -long waveguide electrically connected to a "gain" contact pad. All waveguides in the structure are 2 μm wide with ridges 0.6 μm high. The light reaches the end of the gain guide and travels unguided for 50 μm to the beginning of the bar and cross paths. The input guide, 50- μm unguided region, and the bar and cross path guides form a Y-splitter. The light is split equally into the bar and cross paths. The bar path is formed by an arc of 1.3cm radius, which brings the light to the output end of the switch on the same side it entered. The cross path, which contains two turning mirrors, causes the light to cross to the switch so that it emerges at the output end of the switch on the side opposite from which it entered. By applying a reverse bias to the bar or cross electrical contact pads, the corresponding path becomes opaque so that no light emerges from that path. At the output end of the switch the light again travels through 100- μm

output guides connected to gain contact pads. The switch is symmetric so that light can enter the "output" end and emerge from the "input" end if desired. The switch is designed so that it can be ganged with identical switches to form an NxN switch network.

The turning mirrors accomplish two purposes in this structure. First, they increase the crossing angle between the two cross paths. This is necessary to avoid crosstalk between these two paths as shown below in sec. 7.1.1. The second purpose of the turning mirrors is to widen the switch structure so that the contact pads can be included inside the switch. For a single 2x2 switch this would not be necessary since the pads could be placed on either side of the switch, which would allow the switch to be narrow if required. Most applications for a 2x2 switch require an array of switches to form an NxN switching network. As shown in Fig. 1c, the lateral spacing between switches in such a network is equal to the width of an individual 2x2 switch. For a large network, the electrical contacts must be made to fit within the width of a single switch. The spacing between input and output guides provided by the mirrors is large enough to allow optical fibers to be attached if required, which is an important consideration for some applications. In this design, the electrical contacts are square bonding pads with dimensions of 90 μ m by 90 μ m. As discussed in sec. 8.2, this size could be greatly reduced, which would lead to smaller turning angles in the mirrors reducing the optical loss in the cross paths.

The individual waveguide components of the switch (curved waveguides, Y-splitters, crossovers and turning mirrors) were carefully designed to minimize propagation loss. A short description and analysis of each is given below.

7.1.1. Waveguide Y-Splitters

As already described, the $\Delta\alpha$ switch is formed primarily from four Y-splitters, with the two at the input acting as intensity splitters and the two at the output acting as combiners. A detail of part of the structure containing a Y-splitter is shown in Fig. 24. This shows the gap in the Y-splitter between the single guide input and the two outputs. Also shown is an electrical lead running through a gap in a waveguide as described in sec. 5.2. The electrical lead is identical in structure to the waveguide and is formed at the same time as the waveguides, only the 90° angle between it and the waveguide prevents it from carrying light. The contact pads are put down later in the process and overlap the electrical leads as shown at the right of the figure.

A simplified structure of the Y-splitters is shown in Fig. 26 along with the 2D beam propagator calculation of the optical intensity distribution. The angle of divergence between the two output guides is 2.4° (as in the $\Delta\alpha$ switch). Note that the scale is compressed in the direction of propagation making the angle appear much larger than it actually is. In the splitting mode, light enters from the single guide side. To split the light into two paths it is necessary to widen the mode before entering the two exit guides. This is usually done using a tapered section of guide. In the weakly guiding waveguides used in our designs, we found a taper to be unnecessary. The mode can be widened in the shortest distance by leaving a gap between the input and output guides. In this way, the mode is unguided and diffracts, thus widening as it travels through the gap. Since the difference in effective index between the guides and surrounding area is only 0.1%, there is very little reflection at the guide ends. In the 2D beam propagator calculation, light enters from the straight section of guide at the bottom of the figure. After traveling through the $100\text{-}\mu\text{m}$ input guide, the light emerges into the gap where it expands unguided for $75\mu\text{m}$ before entering the two output guides. As in all the other waveguides in this switch, these waveguides are $2\mu\text{m}$ wide. The narrowest gap between the two output guides is $1\mu\text{m}$, which is about the minimum that can be accurately made using standard contact printing photolithography. The splitting angle was determined using the beam propagator calculation to try various angles to find the maximum angle that had low loss. The configuration used here splits the light evenly into the two paths with 45% in each path and 10% scattered loss (according to the calculation). In the mask set for the switch structure we included some of these Y-splitters so we could evaluate their operation without the complications of the rest of the switch. The measured output from one of these Y-splitters is shown in Fig. 27. The measurement shows that the input is split into two nearly equal modes surrounded by some low level scattered light.

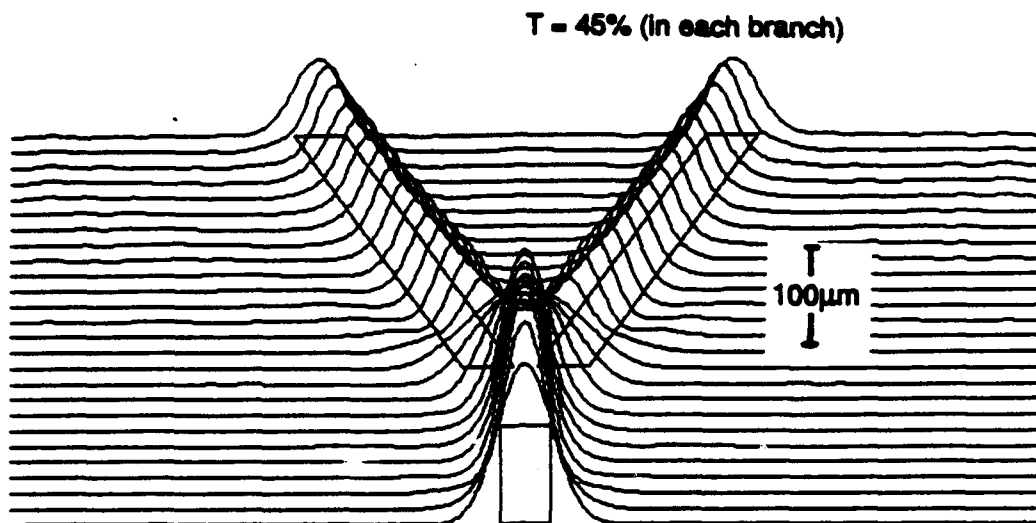


Figure 26. 2D beam propagator calculation of a Y-splitter. The full angle between the two output guides is 2.4° .

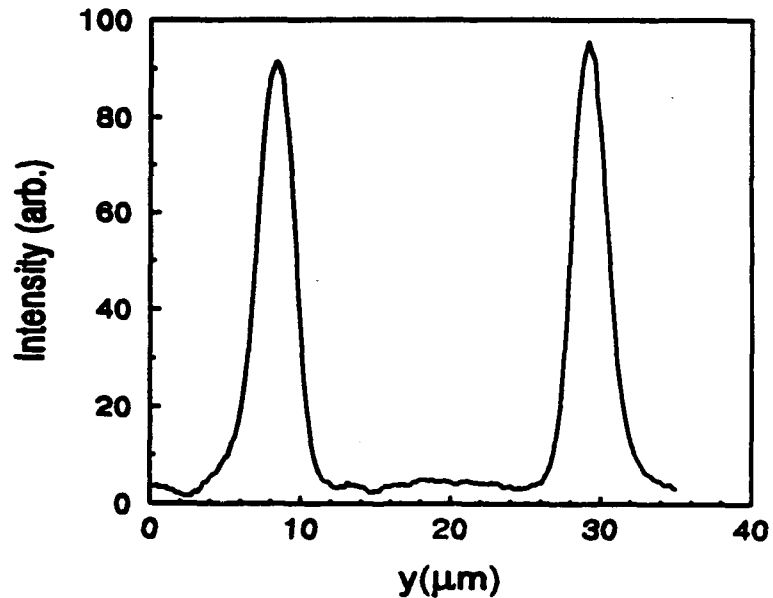


Figure 27. Measured near-field output from a symmetric Y-splitter.

In the actual switch structure, one side of the splitter output goes into a curved guide (the bar path), and the calculation predicts a significant amount of

scattered light outside of the arc path. This scattered light is seen in the measurement of the output intensity of this structure, which is shown in Fig. 28. This measurement was made by cleaving the switch structure down the center leaving the resulting structure shown in the inset in the figure. The output of the curved guide is about 78% that of the straight guide. Since all the symmetric splitters measured had nearly equal intensity distributions between the two guides, we attribute the difference here to losses in the curved section of waveguide so that the transmission in the curved guide is about 78% of that in the straight guide. In this section of switch, the curved waveguide is $300\mu\text{m}$ long, for a full switch the curved waveguides are $600\mu\text{m}$ long so that transmission through the curve in the bar path should be about 60%.

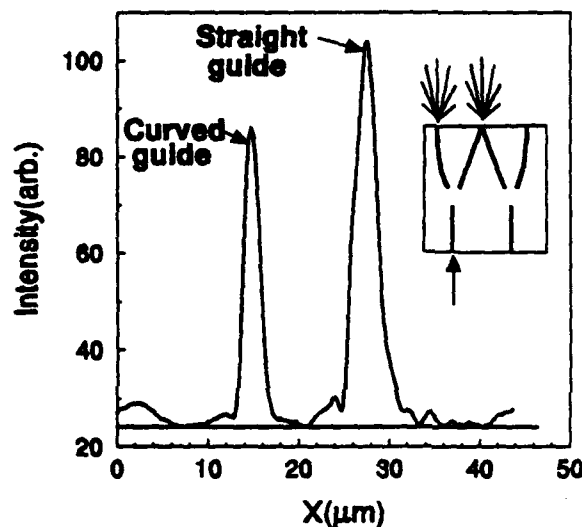


Figure 28. Near-field output from a switch cleaved at the midpoint showing the intensity in the curved guide (bar path) and straight guide (cross-path).

In addition to the symmetric Y-splitters used in the switch, we included an asymmetric Y-splitter in the test structures included in the switch mask set. These were included for possible use in future switch designs. The structure of the asymmetric splitter and the beam propagator calculation are shown in Fig. 29. The structure consists of a single input guide, a parallel output guide (parallel to the input guide) and an angled output guide. In a switch, this would eliminate the need for curved bar paths, which can be lossy as demonstrated above. In the beam propagator calculation the output intensity of

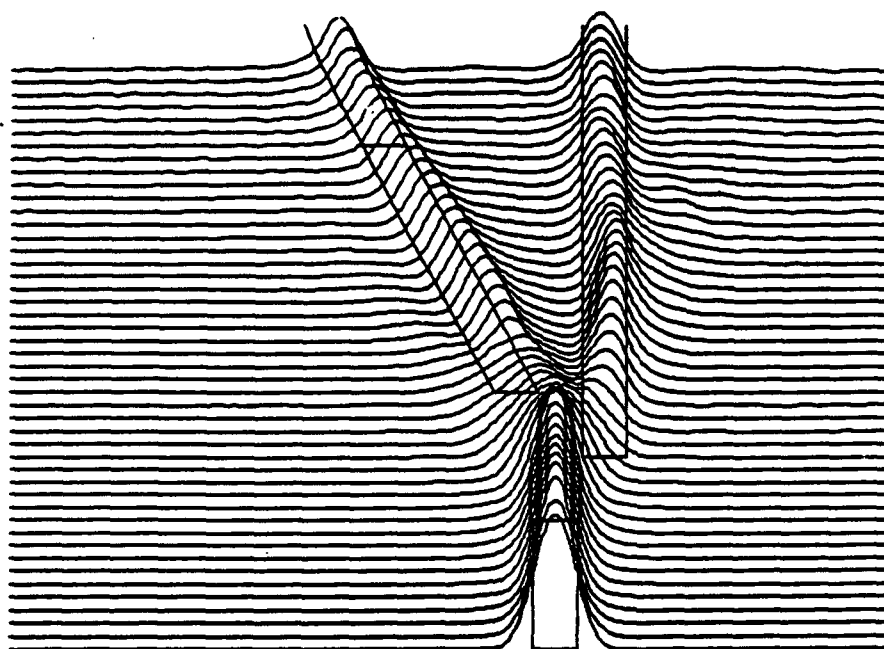


Figure 29. Asymmetric Y-splitter structure and the 2D beam propagator calculation of its operation. The predicted intensity from the 2° angled guide is 89% of that from the straight guide.

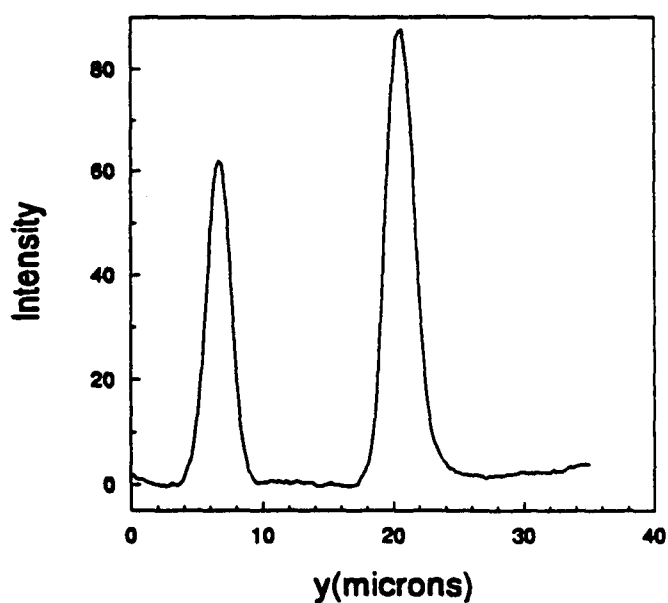


Figure 30. Measured output from the asymmetric Y-splitter. The measured intensity from the angled (left) guide is 71% of that from the straight (right) guide.

the angled guide is about 89% of that of the parallel guide. In the measurement shown in Fig. 30, the intensity of the angled guide is about 71% that of the parallel guide. With further work, it should be possible to make the outputs of this splitter nearly equal in intensity.

7.1.2. Waveguide Crossovers

At the center of the switch is the crossover between the two cross paths. Without the turning mirrors, the angle between the crossing guides would be about 2.4 degrees, which is determined by the splitting angle of the Y-splitters. To analyze waveguides intersecting at that angle, we used the 2D beam propagation program. The calculation for an ideal pair of waveguides crossing at 2.4 degrees is shown in Fig. 31a. The crosstalk between the guides in this calculation is only 4%, which would be acceptable for many applications. This assumes a perfect structure with a sharp intersection where the guides meet, which would be impossible to fabricate. A more realistic structure is shown in Fig. 31b. In this structure the sharp intersections have been squared off so that the smallest dimension is $1\mu\text{m}$, which is closer to what can actually be achieved using standard photolithography techniques. In this case, the 2D beam propagator program finds about 13% crosstalk, which is above acceptable levels. To eliminate the crosstalk problem at this crossing, we incorporated turning mirrors into the switch structure. With the addition of turning mirrors, the angle between the two crossing guides is near 90 degrees, which virtually eliminates crosstalk between these guides.

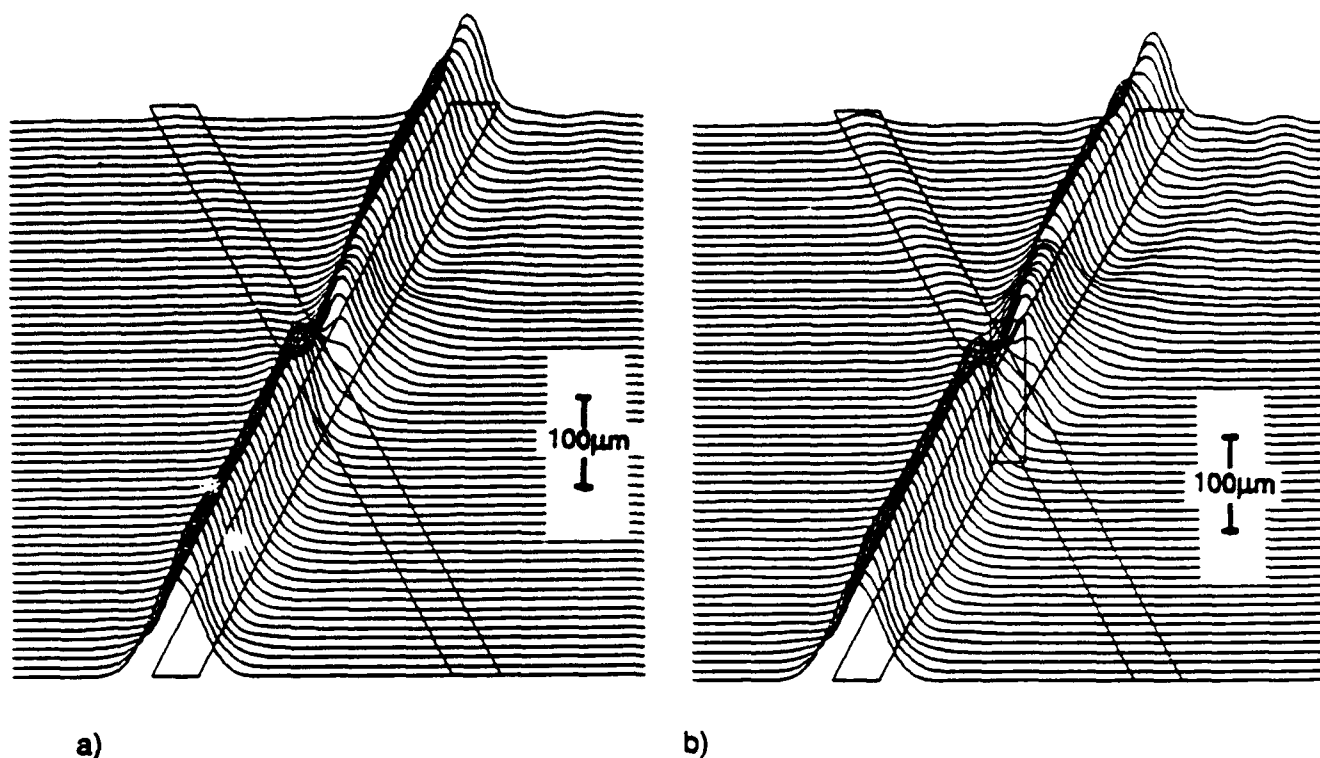


Figure 31. Waveguides crossed at 2.4° . In (a) the intersection is perfectly sharp. In (b) the intersection is cut off at $1\mu\text{m}$, which is closer to a real structure

7.1.3. Waveguide Turning Mirrors

An important component of the $\Delta\alpha$ switch is the turning mirror. Turning mirrors were included in the structure to both reduce crosstalk between the two cross path guides and to make the switch structure wide enough to provide room for the electrical contacts. The basic idea behind the turning mirror is to use a deeply etched trough to create a GaAs/air interface. Light hitting this interface at greater than the critical angle will be totally reflected. By proper positioning of the input and output guides with respect to the mirror interface, a low loss turning mirror can be formed. In practice there are several loss mechanisms that can greatly reduce the efficiency of the turning mirror. Some of the loss mechanisms are: 1) misalignment between the waveguides and the mirror interface, 2) diffraction losses due to unguided propagation within the mirror structure, and 3) scattering due to roughness at the mirror interface.

A detailed drawing of the turning mirror structure is shown in Fig. 32. As with all the waveguide structures in the switch, the waveguides are formed by first putting down the metal patterns and then using those metal patterns as a mask in a reactive ion etch process. To form an accurately aligned mirror edge, we use a self-aligned process to etch both the waveguides and the mirror.¹⁰ In

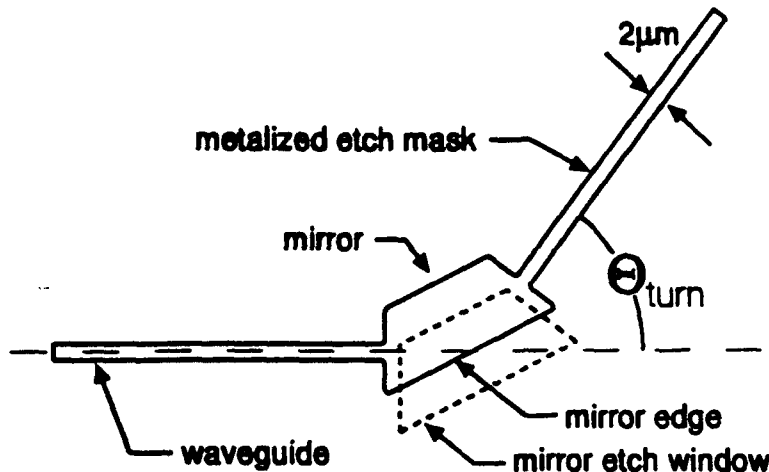


Figure 32. The self-aligned turning mirror structure used in the $\Delta\alpha$ switch.

this process the metal is put down in the pattern shown in Fig. 32. This pattern defines both the input and output waveguides as well as the mirror edge. Since the mask used to form this pattern is made using e-beam lithography, the angles and dimensions of this structure are extremely accurate (to about $0.1\mu\text{m}$). Following the metal application, the waveguides are formed using the standard waveguide etch of about $0.5\mu\text{m}$, which forms all the waveguides in the structure. After the waveguides are formed, photoresist is spun over the structure and windows are opened over the mirror edges (mirror etch window shown in Fig. 32). A second etch is then used to form a deep trough in the area not covered by either photoresist or metal. Since the mirror edge is formed by the original metal that also defines the waveguides, it is precisely aligned with the waveguides. An SEM micrograph of one of the self-aligned mirrors is shown in Fig. 33.

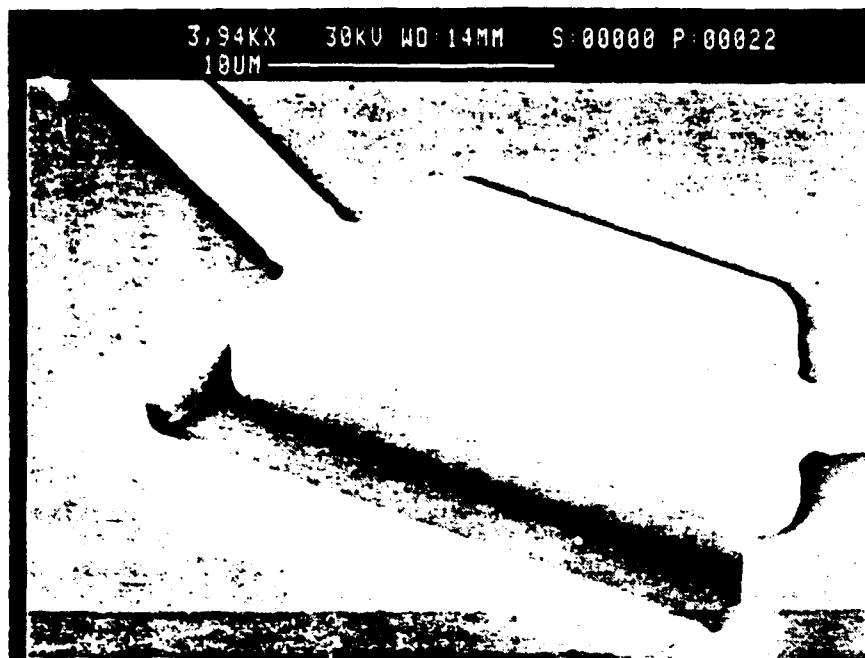


Figure 33. SEM micrograph of the self-aligned mirror structure.

To test the turning mirrors, we included a series of mirror tests paths on the switch mask sets. The test paths from the second switch are shown in Fig. 34 (the first switch contained a single test path). The test paths consist of a single straight path for reference and three mirror paths containing four turning mirrors each. The turning angles of the four mirrors within a single mirror path are identical. The mirror angles for the three mirror paths are 37° , 53° , and 90° . These angles were chosen because the e-beam lithography machine that draws the masks uses a square writing grid. For this reason angles with integer (or one over integer) tangents are drawn more smoothly than arbitrary angles. (Note that the mirror angle is one half the turning angle so the turning angles of 90° , 53.1° and 36.9° correspond to mirror angles of 45° , 26.6° , and 18.5° , which have tangents of 1, $1/2$, and $1/3$, respectively.) The unguided lengths in each mirror structure are $30.6\mu\text{m}$, $22.8\mu\text{m}$ and $15\mu\text{m}$ for the 37° , 53° , and 90° mirrors, respectively. The calculated diffraction losses, determined using the beam propagator, for these mirrors are 4%, 0.2% and 0.1% for the 37° , 53° , and 90° mirrors, respectively. Measurements of the losses were made by comparing the intensity output of each mirror path with the output of the reference path. The transmission determined from each path was then assumed to be the fourth

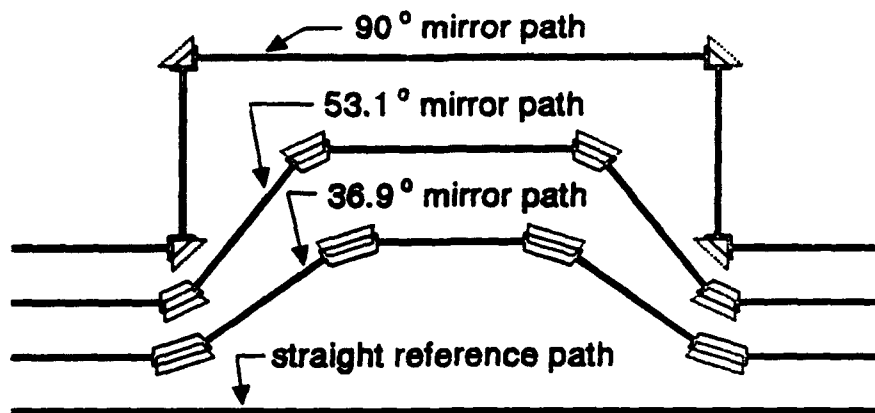


Figure 34. Test path used to determine the loss of turning mirrors fabricated for different turning angles.

power of the mirror throughput since each path contained four mirrors. Figure 35 shows the measured output intensity profiles for one of these measurements. The experimentally determined mirror reflectivities are $84 \pm 4\%$, $75 \pm 8\%$ and $41 \pm 9\%$ for the 37° , 53° , and 90° mirrors, respectively. The mirrors used in the switch were 45° in the first design and 53° in the second design. (The design was changed after the first version to use angles that could be drawn more smoothly in the mask making process.) Since each cross path contains two mirrors, the transmission of the cross-path should be about 50% of that of the bar path due to mirror losses, though the 60% transmission through the curved bar guides nearly balances out this loss.

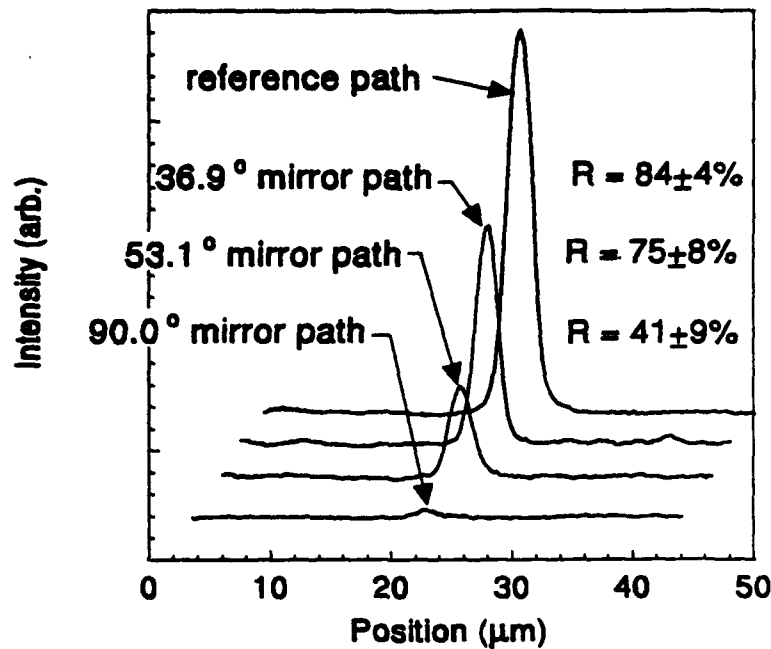


Figure 35. Near-field intensity output from the four test mirror paths. All four curves are plotted on the same intensity scale but offset for clarity.

7.1.4. Curved waveguides

As shown in Fig. 23, each bar path contains a curved section of waveguide. In both $\Delta\alpha$ switch designs fabricated in this program, the radius of these curves is 1.3cm. This curvature, the length of the bar sections and the splitting angle of the Y-splitters are all interrelated parameters. Since we wanted to keep the overall length of the switch at about 1mm, and the gain sections at each end are 100 μ m long, the length of the bar section is 600 μ m.

A 2D beam propagation calculation of a curved section of the waveguide is shown in Fig. 36. The calculated transmission through the 600- μ m-long, 1.3-cm-radius guide is 92%.

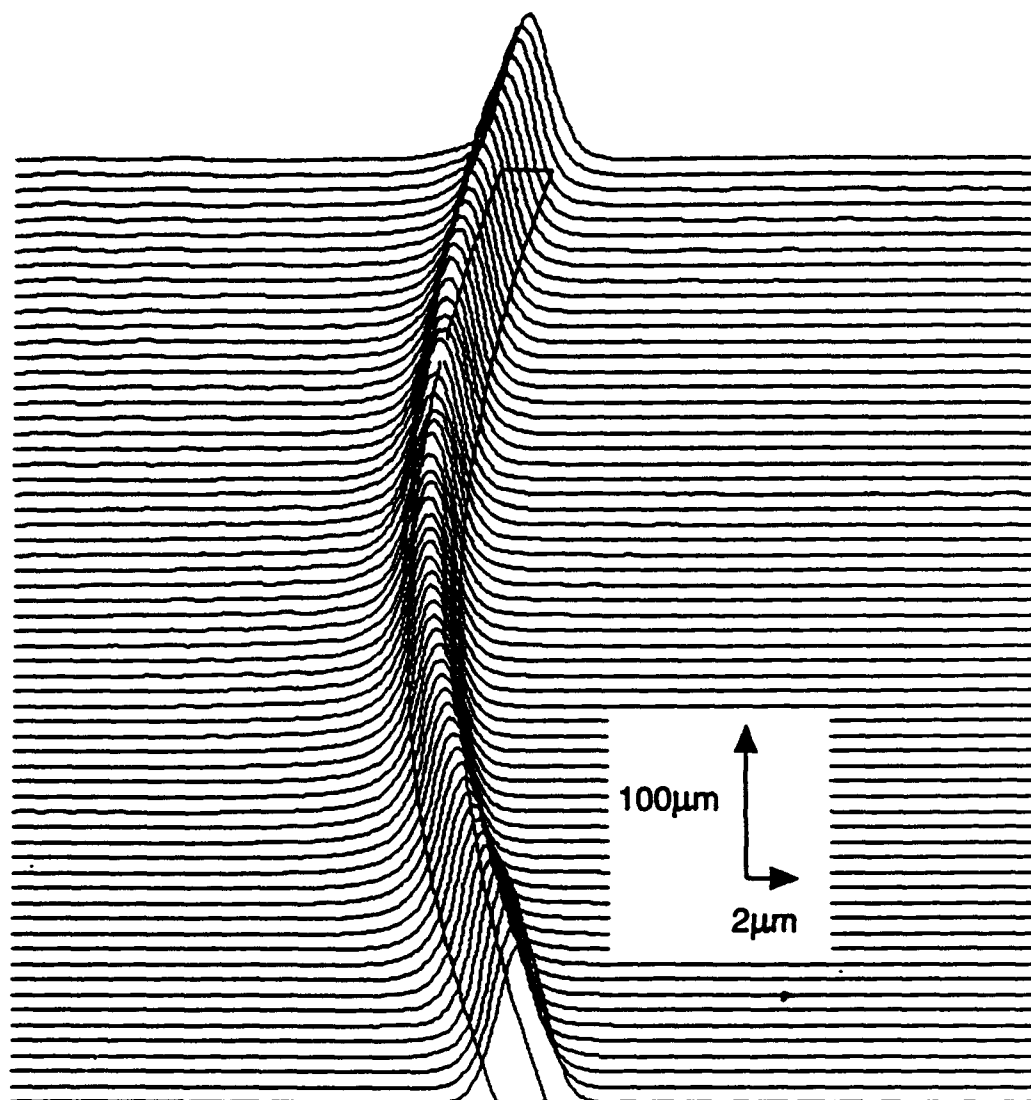


Figure 36. 2D beam propagator calculation of the 1.3-cm-radius arc used in the bar path of the $\Delta\alpha$ switch.

7.2. 2 x 2 $\Delta\alpha$ Switch without Gain

Two designs of the $\Delta\alpha$ switch were made during the development process, the first, which is described in this section, incorporated all of the major features described above, but did not have gain. The structure of this switch is shown in Fig. 37, a micrograph of the structure is shown in Fig. 38. As shown in the diagram, the switch has separate electrical contact pads for each gain section (which were never used in this design), and one electrical contact pad each for the bar and cross paths. The total length of the switch is 960 μm.

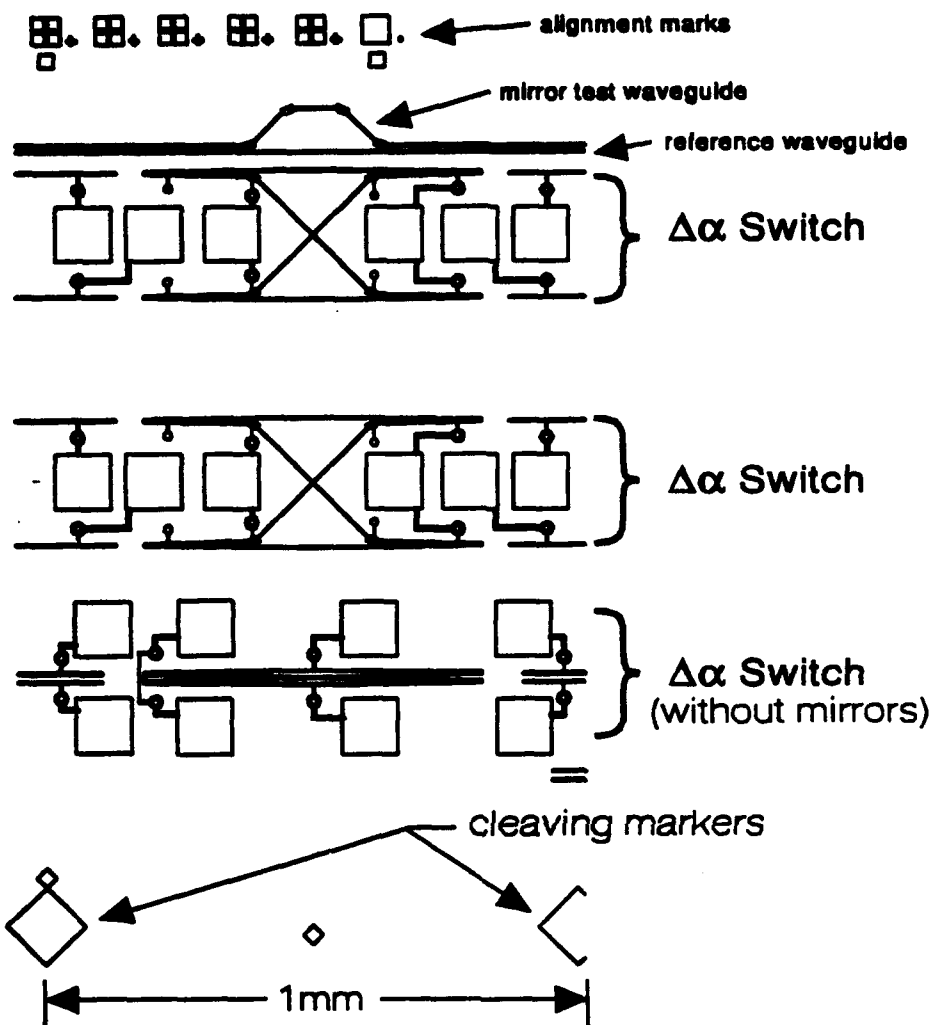


Figure 37. Layout of the $\Delta\alpha$ switch and test structures.

The switches are arrayed in groups of six to form a 4x4 switch network, which is only partially shown here. Also shown at the bottom of the micrograph (Fig. 38) are several switches that contain no turning mirrors thus making them much more narrow and requiring the electrical contact pads on the outside of the switch structure. Because the electrical contacts are in the way, these switches could not be arrayed in a network. Tests of these narrow switches showed severe cross-talk problems so this design was not pursued any further. Shown

above the switches in the micrograph is a single mirror test path along side a straight reference waveguide. For test measurements, the structure shown in the micrograph was cleaved along vertical lines running through the diamonds at the bottom of the micrograph. This allowed measurements on single switches and single sets (groups of four) of test mirrors. The mirrors in this structure had reflectivities of about 63%.

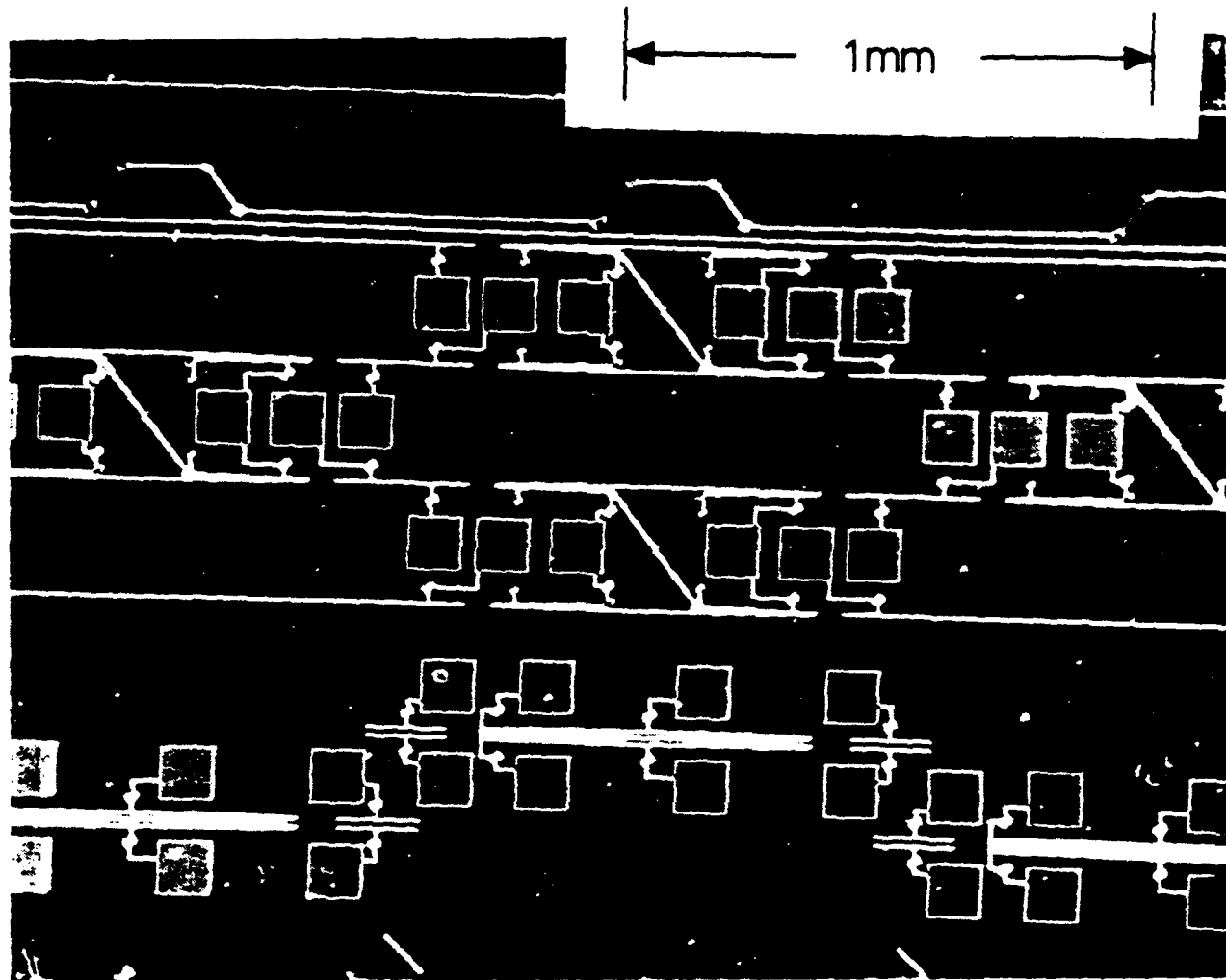


Figure 38. SEM micrograph of the $\Delta\alpha$ switch.

The near field output of the switch is shown in Fig. 39. This figure shows the output intensity profile for three different states of the switch. The bottom trace shows the output with no bias on either the bar or cross paths. Input is on the left side as shown on the inset in the figure. The peak on the left side has a large amount of scattered light surrounding it, which is presumably caused by

light scattering out of the curved section of waveguide. The middle trace shows the output with -9V bias on the cross guide. In this case, the right peak intensity is zero (to the precision of the measurement). Finally, the upper trace shows the output with -9V on the bar paths. In this case the central peak is eliminated, but the scattered intensity remains.

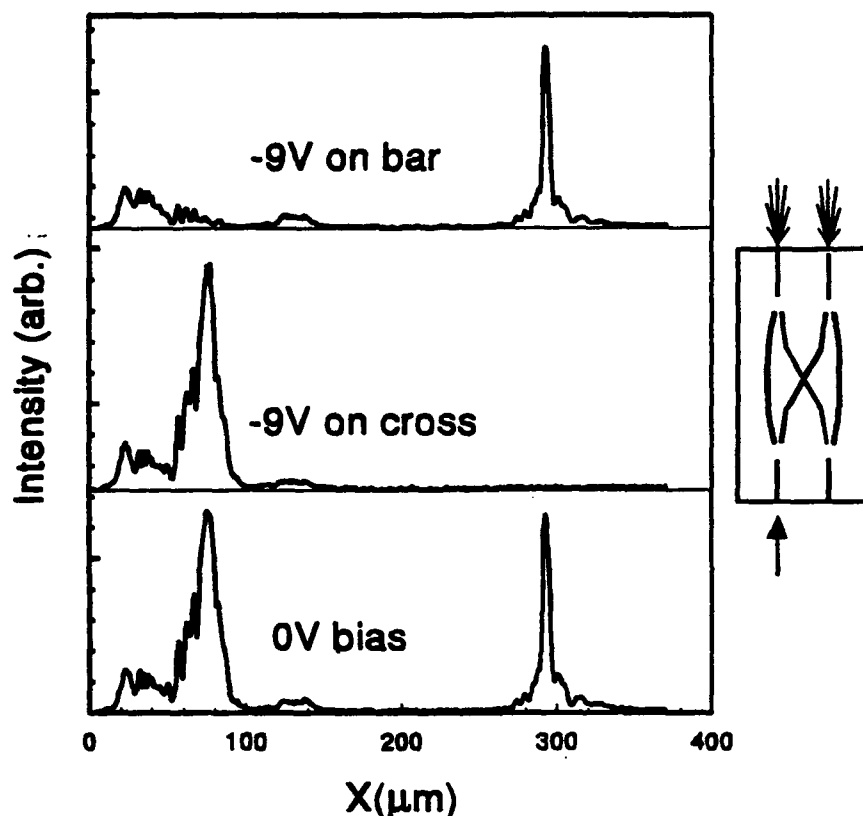


Figure 39. Near-field output from the $\Delta\alpha$ switch under three bias conditions.

7.3. Using Disordering to Combine Gain and Modulation

As described in the introduction to section 7, the requirement to have gain producing waveguides in the switch necessitates blue shifting the rest of the waveguides in the switch. To accomplish this, we chose to use oxide induced disordering to blue shift the quantum well excitons in selected areas of the switch. Disordering blue shifts the quantum well exciton by diffusing the

quantum well structure and raising the energy level of the wavefunctions in the quantum well. An example calculation showing this effect is provided in Fig. 40. Figure 40a shows the conduction band quantum well with its calculated ground state exciton. The quantum well is a 100Å wide GaAs layer surrounded by $\text{Al}_{0.3}\text{Ga}_{0.7}\text{As}$. In this structure, the conduction band well is about 300meV deep with the ground state level about 61meV above the bottom of the well. Figure 40b shows the same quantum well after diffusion. In this case, Al diffuses into the well, raising the ground state energy level, thus shifting the absorption toward the blue. The calculated diffusion of the well structure for an integrated diffusion time product of 150\AA^2 is shown on the right of the figure. Both sets of plots in the figure are on the same vertical energy scale, and the wavefunctions are plotted on baselines equal to their energy levels. The upward shift in the ground state wavefunction between the as-grown well and the diffused well is due to the change in the well, which raised the wavefunction energy by 12.9meV.

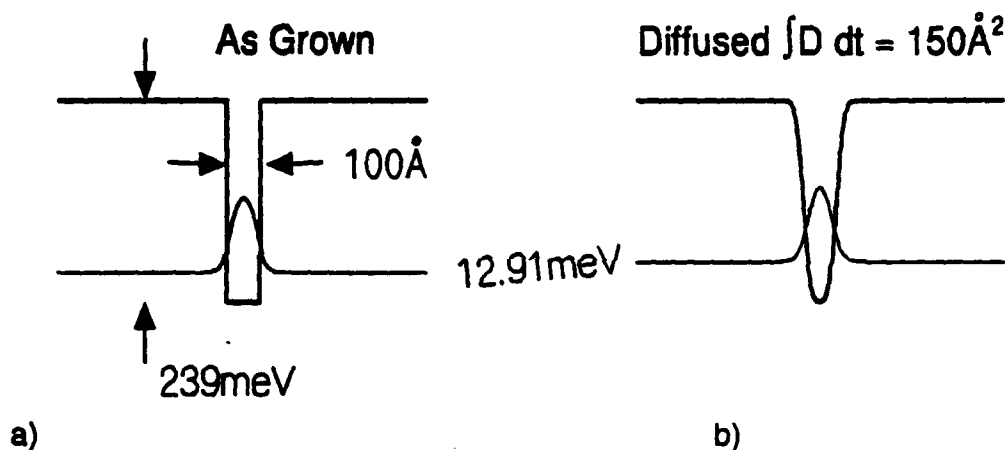


Figure 40. Calculated effect of diffusion on a quantum well and its ground state energy.

In a real device, the disordering process is accomplished by covering the surface of the area to be shifted with SiO_2 . The wafer is then placed top side down on another GaAs wafer forming a proximity cap, which prevents out-diffusion of As from the uncoated areas of the wafer. The two wafers are then placed in a rapid thermal anneal at approximately 960°C for 60 to 90 sec. (These parameters vary depending on the waveguide structure and the amount of shift required.) An example of the results of this process is shown in Fig. 41. The figure shows photocurrent spectra of three samples taken from the same wafer. The three traces in the figure show spectra of the as-grown quantum well with a peak at 8502Å, a proximity capped area with a peak at 8462Å and an oxide disordered area with a peak at 8308Å. The waveguide structure used in this measurement contained 10 quantum wells in the 0.2-μm-thick core. Since

the blue shifted peak is only slightly broadened, the effect of the disordering must be nearly equal over the thickness of the waveguide core ($0.275\mu\text{m}$).

Measurements of the Stark shift of an as-grown sample (control) and disordered sample (VID) are shown in Fig. 42. Application of a 10V reverse bias to the control sample shifts the excitons by 90A while the same bias applied to the VID sample shifts its excitons by only 38A. We believe this reduction in the Stark shift is because the shape of the disordered well approximates a parabola. Excitons in a perfect parabolic well would not be shifted by an external field. Further development of the model calculation for disordered wells should allow this reduction in Stark shift to be modeled. Careful design of a pair of coupled wells should make it possible to achieve sufficient Stark shifts in the disordered

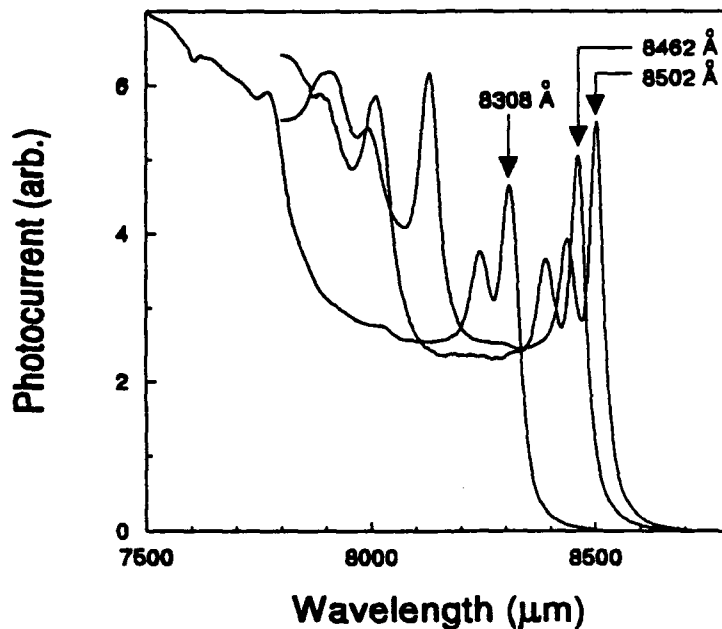


Figure 41. Photocurrent spectra of a waveguide sample containing SQW's. The peaks at 8502A, 8462A and 8308A correspond to the as-grown, proximity capped and vacancy induced disordered material, respectively. The anneal for VID was 960 °C for 90 s.

ACQW structure, though it is probably not possible to maintain large Stark shifts in a disordered simple square quantum well.

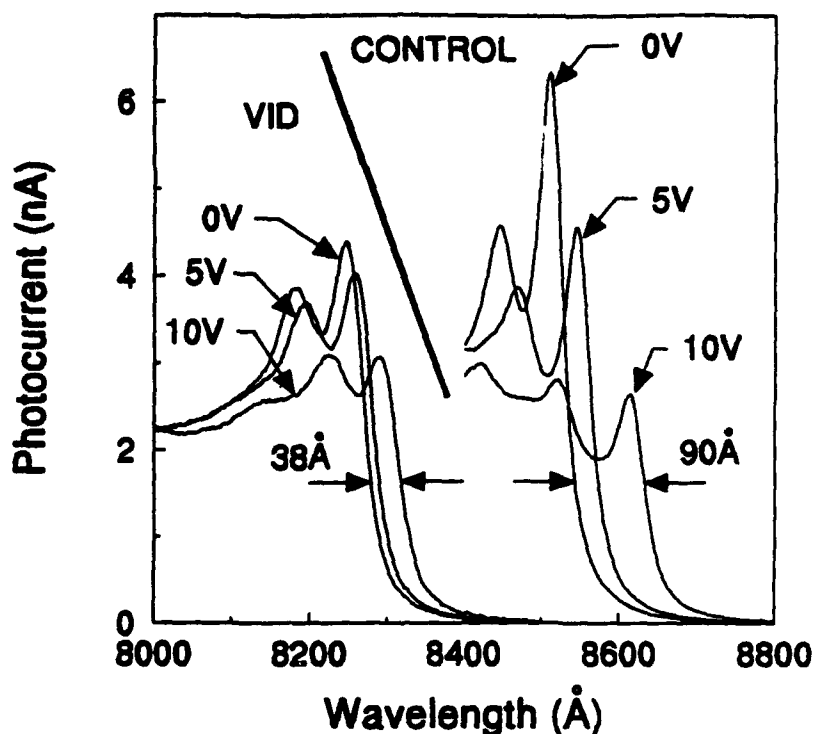


Figure 42. Measurement of the Stark shift for 100Å wells with (VID 960 °C for 90 s) and without (control) vacancy induced disordering.

To determine the proper annealing parameters, it would be desirable to develop a model that could predict the amount of energy shift for a given set of processing parameters. However, this would require a large effort and is beyond the scope of this program. Instead, the approach we took was to disorder single quantum well structures to determine the integrated diffusion. By repeating the calculation shown in Fig. 40 for both the conduction and valence bands, the wavelength shift as a function of integrated diffusion was determined. An example of this calculation is shown in Fig. 43. Using this curve, the measured wavelength shift can be used to determine the diffusion parameter for the calculation. This can then be used to calculate the effects of the disordering process on the ACQW's in the waveguide. A diffusion parameter of 150\AA^2 is required to produce the necessary shift between the proximity capped and oxide disordered region of the switch. The calculated wells and wavefunctions of the ACQW structure before and after disordering are shown in Fig. 44. The important result is that the well remains well defined so that the first two wavefunction are still qualitatively the same as those in the as grown ACQW. This ensures that the structure has the indirect transition required for the ACQW operation.

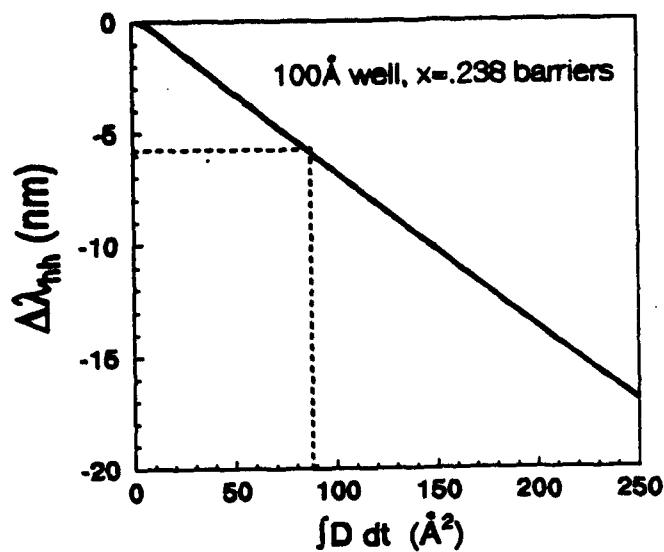


Figure 43. Calculated exciton wavelength shift as a function of diffusion for a 100 Å quantum well.

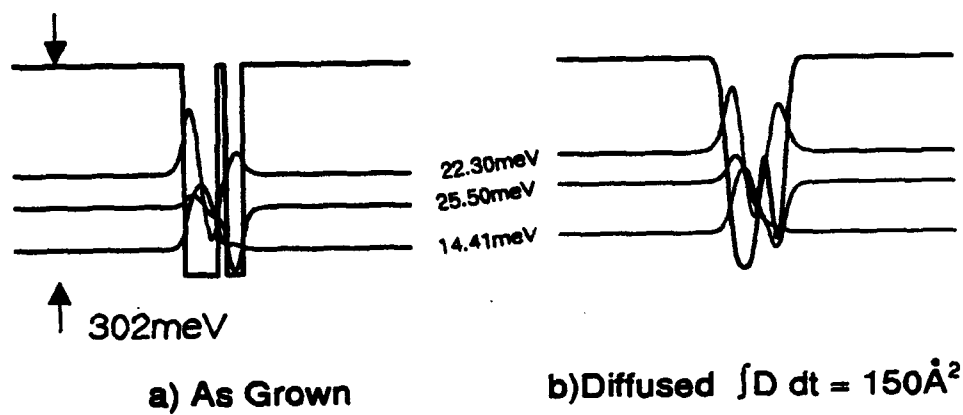


Figure 44. Calculated effects of diffusion on an ACQW structure and its energy levels.

7.3.1. Electrical Measurements on VID diodes

To determine the electrical effects of the VID process, if any, on the diode waveguide structures, the material was divided into three pieces. One piece was used as a control sample; another was proximity capped and RTA'd; and a third was coated with oxide and RTA'd. Each of these pieces was then processed into 250- μm -diameter mesas with electrical contacts in preparation for electrical measurements. Two wafers, one with a waveguide containing 10 SQWs in the core and a second with 10 pairs of ACQWs were prepared in this way. The results of electrical measurements are shown in table II. Though there are some small changes in the electrical characteristics, these should not affect the operation of the $\Delta\alpha$ switch.

Table II. Electrical properties of disordered waveguides
(annealing parameters : 960 °C for 90 s)

<u>SQW sample</u>	Forward bias turn-on (V)	Resistance (after turn-on)	Reverse bias breakdown (V)	Current @-15V(mA)
control	1.57	17.6 Ω	-51.0	-1.7
prox. cap	2.24	21.4 Ω	-48.0	-1.7
VID	1.68	12.4 Ω	-28.0	-1.6

<u>ACQW sample</u>	Forward bias turn-on (V)	Resistance (after turn-on)	Reverse bias breakdown (V)	Current @-15V(mA)
control	1.54	11.8 Ω	-49.5	-2.0
prox. cap	2.36	19.0 Ω	-27.5	-1.7
VID	1.71	18.0 Ω	-27.5	-9.3

7.4. 2 x 2 Switch with Gain

The final switch made in this program was the 2x2 $\Delta\alpha$ switch with gain. A diagram of this switch is shown in Fig. 45. The structure is nearly the same as that described in the previous section except that there is only one electrical contact pad for gain at each end of the switch, and the width of the structure has been reduced. The most significant change is the VID boundary around the

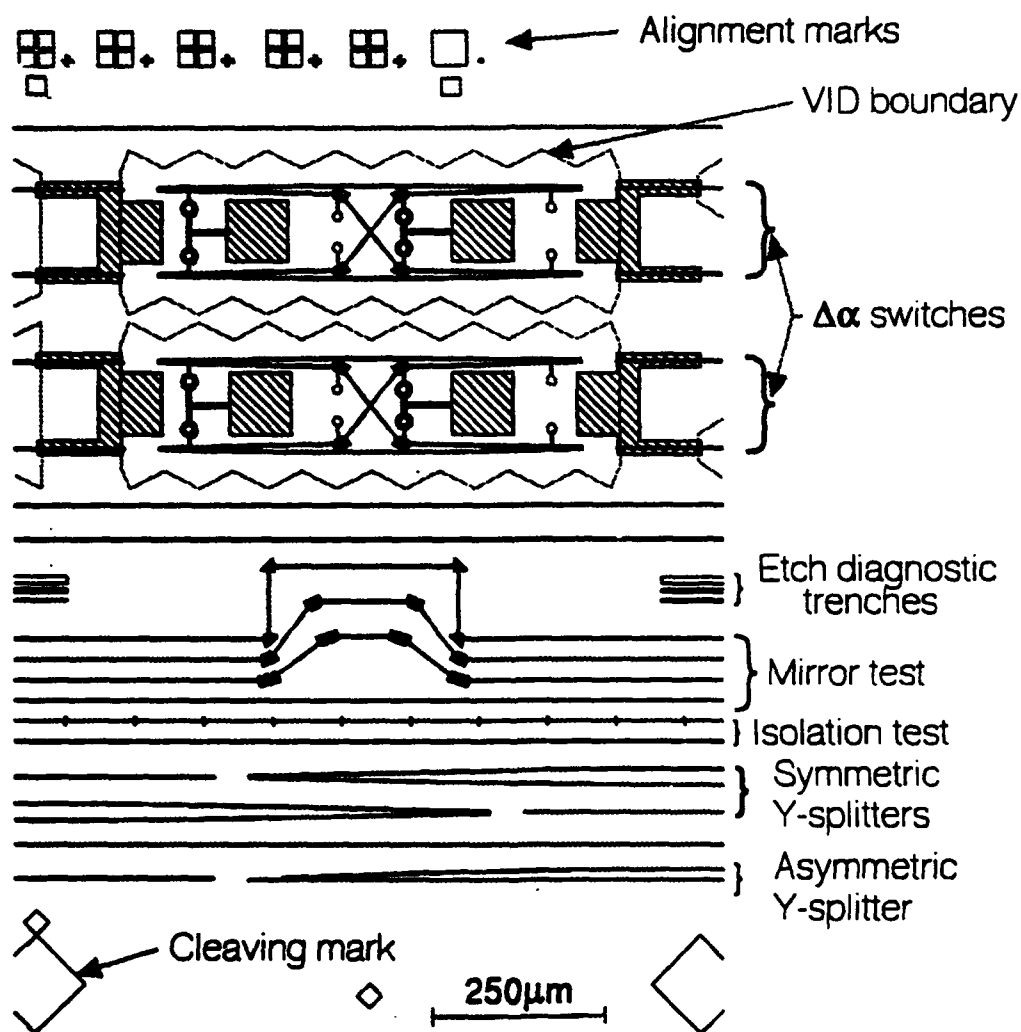


Figure 45. Second design for the $\Delta\alpha$ switch, which includes vacancy induced disordering regions.

central area of the switch. As the first step in the processing of the switch, this area is covered by SiO_2 and the wafer is then annealed to produce the oxide disordering shift. An electron micrograph of the switch is shown in Fig. 46. Also shown in this micrograph are a series of test structures that were included in the design. These test structures include the asymmetric Y-splitter, symmetric Y-splitters, a waveguide with 4- μm gaps, a waveguide with 4- μm gaps with crossing waveguides, and a series of mirror test paths. All of these test structures have been discussed in previous sections.

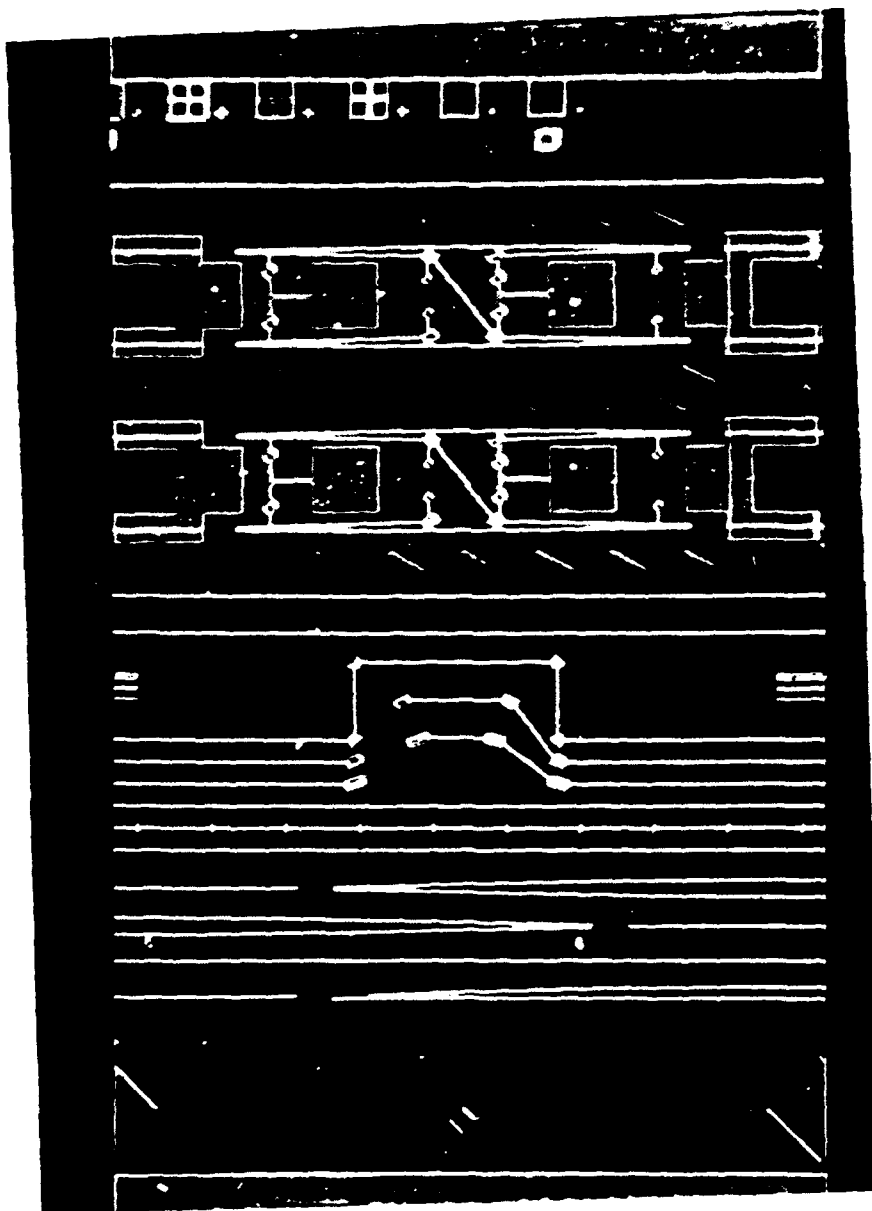


Figure 46. SEM micrograph of the $\Delta\alpha$ switch.

The structure also contains several straight reference guides, both disordered and proximity capped. Figure 47 shows waveguide output from both types of reference guides, first at 861.9nm where both are transparent (top two plots in the figure). The bottom pair of curves shows the output from the two guides at a shorter wavelength. This pair of measurements shows the decreased transmission of the proximity capped guide relative to the disordered guide. By repeating these measurements over a range of wavelengths, we determined the transmission through each waveguide as a function of wavelength. The results are shown in Fig. 48. Through a different set of measurements, we determined that the coupling loss at each end of the waveguide is about 60%. This includes the 30% reflection at each end and the mismatch between the coupling optics and the waveguide. This means that the zero propagation loss level on this plot would correspond to about 16% transmission. The apparent noise in both curves above the 10% transmission level is due to interference between the two ends of the switch (which was about 1mm long), indicating the propagation loss through the switch was low. The two curves are shifted by 6.9nm due to the vacancy induced disordering. This shift is smaller than ideal since the gain in the proximity capped guide occurs at 855nm. At that wavelength the transmission through the oxide disordered guide is only about one-fifth of what it would be for a 15- to 20-nm shift.

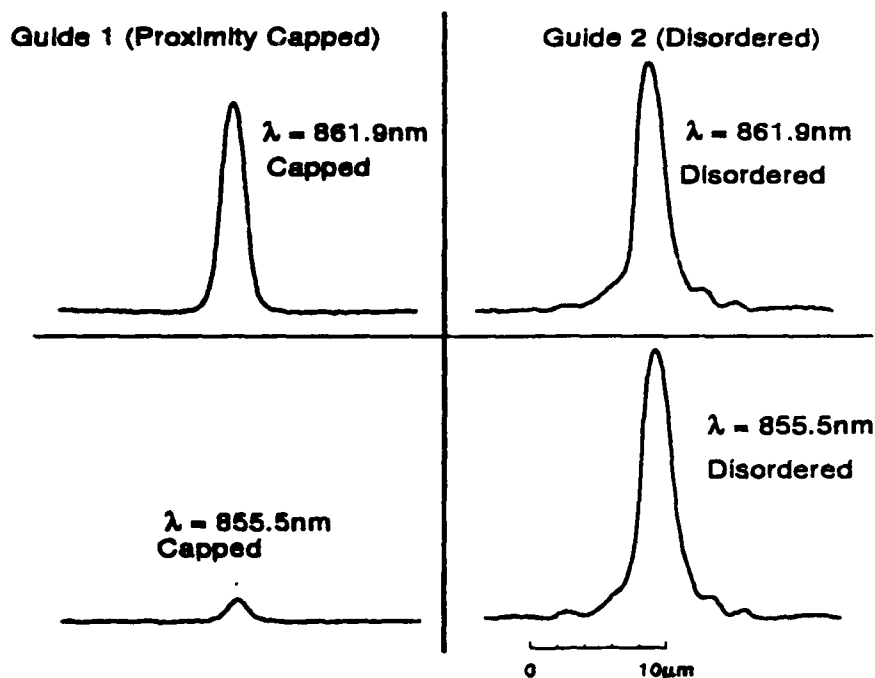


Figure 47. Comparison of transmission through proximity capped and disordered waveguides at two wavelengths. VID annealing parameter: 950 °C for 60 s.

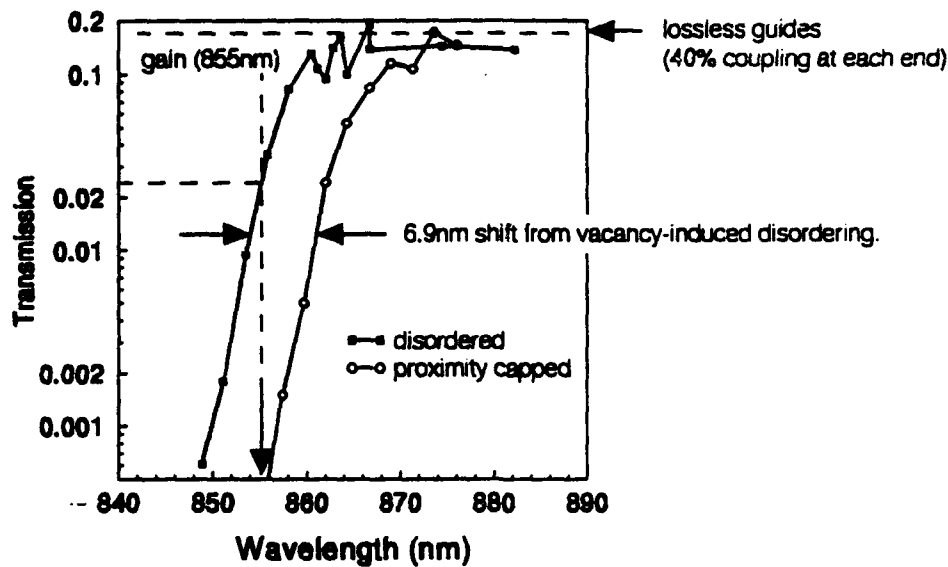


Figure 48. Comparison of the transmission through proximity capped and disordered waveguides as a function of wavelength. Annealing parameters: 950 °C for 60 s.

7.4.1. Verification of Gain by Laser Measurements

To verify that the proximity capped waveguides do produce optical amplification when forward biased, a series of laser measurements were made using a laser diode characterization station, which is used to test lasers fabricated at the Laboratories. Measurements were made on forward biased straight waveguides alongside the switch structure. These waveguides are shown in Fig. 45 with a single waveguide above the $\Delta\alpha$ switch structures and two below the $\Delta\alpha$ switch structures. Since there are no contact pads on these guides, a small amount of silver epoxy was put over each guide to allow contact by a micro-probe. Figure 49 shows the measured instantaneous output intensity from several guides as a function of the current into the guide. For all of these laser measurements, the current was applied as a 500-ns pulse at a 5-KHz repetition rate, resulting in a 0.1% duty cycle. Curves are shown for both the SQW and ACQW waveguides. The sharp turn on in each curve is characteristic of lasing action in the waveguide. To further verify lasing, spectral measurements were made of each of these guides with the results shown in Fig. 50. The narrow bandwidth of these spectral modes is also an indication of laser action. To determine the bandwidth of the gain, a final set of spectral measurements was taken of the forward biased gain sections at the ends of the switch (see Fig. 45). Since these gain sections have only one cleaved end, they

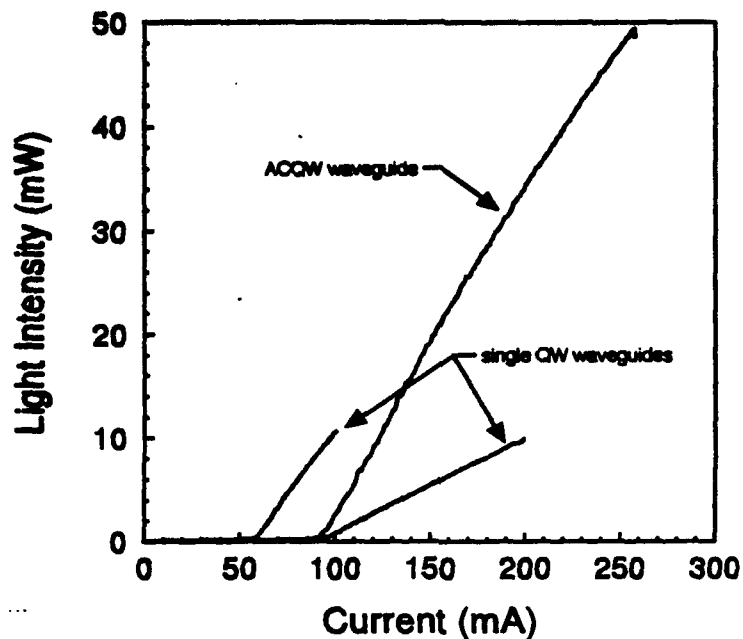


Figure 49. Light output vs. forward bias current from the straight 1-mm-long proximity capped waveguides included in the $\Delta\alpha$ switch test structures.

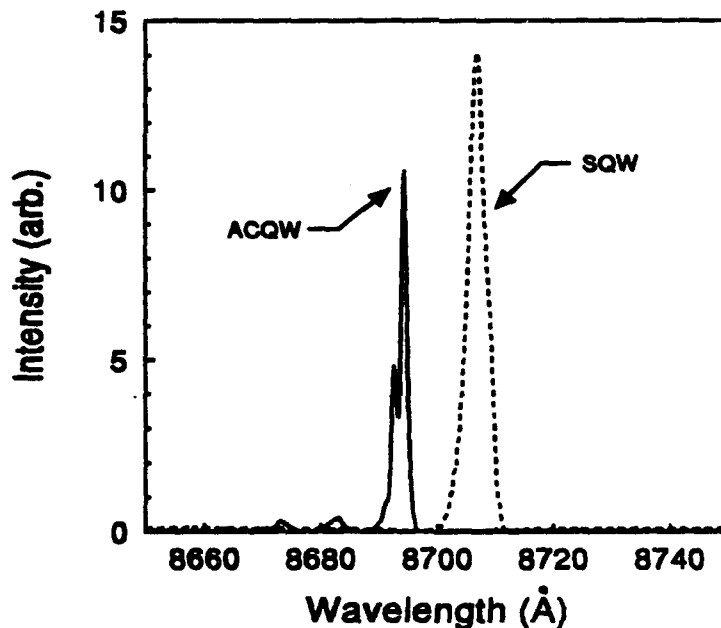


Figure 50. Spectral output of forward biased proximity capped waveguides.

cannot lase, so the output will show only the spontaneous emission, which is proportional to the gain. These spontaneous emission spectra for both SQW and ACQW waveguides are shown in Fig. 51. These curves show that the gain can be achieved over a relatively broad band approximately 750Å wide.

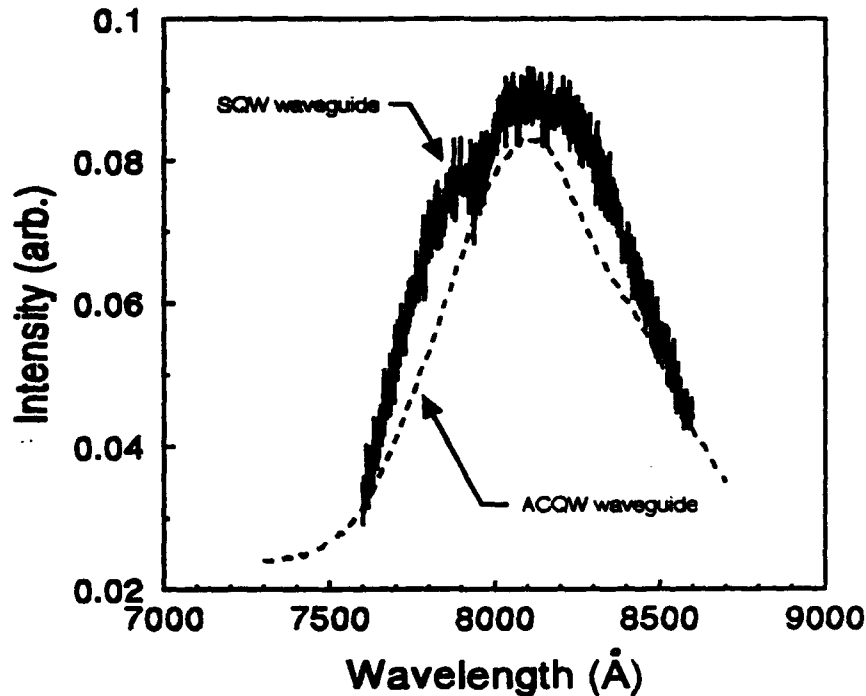


Figure 51. Spontaneous emission from the forward biased gain sections at the input of two switches.

The results of these measurements clearly show that the proximity capped waveguides act as lasers when forward biased. Since a laser can only operate if there is gain in the resonator, it is clear that the proximity capped waveguides produce gain when forward biased.

7.4.2. Measurement of the $\Delta\alpha$ Switches with Gain

The measured transmission, including gain, for both the bar and cross paths of a switch containing a single quantum well is shown in Fig. 52. In this measurement, only the propagation loss through the switch is included; the coupling losses at the ends of the switch were eliminated. (Coupling losses at the facets were determined from transmission measurements through a short straight waveguide at a longer wavelength). The propagation loss through the switch is the important parameter for a network where there would be no additional facet coupling loss between switches. Coupling loss at each end of a

switch network could be corrected using anti-reflection coatings, fibers that efficiently couple to the waveguide modes, and additional gain. The curves shown in Fig. 52 were measured at a wavelength of 855nm where the gain was at its peak. This measurement was made using a 5% duty cycle in the current supply. Transmission through this switch with gain sections biased approached 40% for the bar path and 20% for the cross path (which has higher losses due to the turning mirrors).

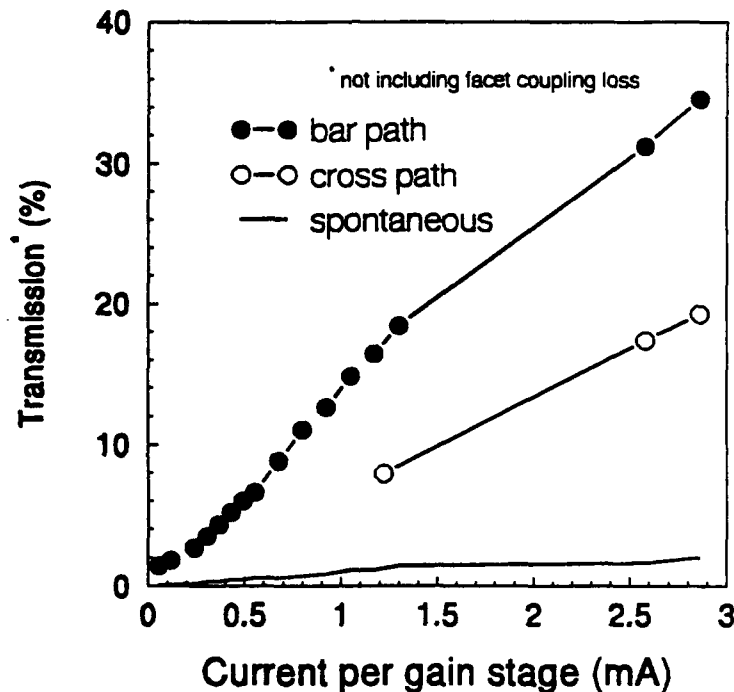


Figure 52. Measured output from a $\Delta\alpha$ switch as a function of forward bias current to the gain stages.

A final switch using the ACQW structure with VID was fabricated near the end of the program. For this switch the ACQW structure was changed from the standard structure (100Å and 50Å wide wells separated by a 25Å wide $\text{Al}_{0.3}\text{Ga}_{0.7}\text{As}$) to a modified ACQW structure (100Å and 67.5Å wide wells separated by a 20Å $\text{Al}_{0.35}\text{Ga}_{0.65}\text{As}$ barrier). This modified ACQW is the one shown in Fig. 44 and was designed so that the well would maintain the ACQW characteristics after disordering. Because the SQW switch was shifted by only 6.9nm in the disordering process (see Fig. 48) using an anneal of 950 °C for 60 s, the ACQW was annealed at 960 °C for 90 s.

Figures 53 and 54 show this switch in operation. Figure 53 shows a switch with no wires attached, but with light entering the lower left input of the top switch. Scattered light can be seen (from left to right) at the input, a Y-splitter, the first turning mirror, the second turning mirror, a second Y-splitter (combiner) and at the two outputs of the switch. Figure 54 shows an identical switch with wires attached and current supplied to the gain sections. In this case, light is entering the top left input of the switch.



Figure 53. Micrograph of an ACQW switch with light entering the lower left input of the top switch.



Figure 54. Micrograph of an ACQW switch with light entering the upper left input of the top switch. Current supplied to the gain sections causes them to glow.

Transmission measurements for the ACQW $\Delta\alpha$ switch with gain are shown in Fig. 55. These measurements were made using a 0.6% duty cycle current pulse. Both outputs of the switch were focused on the detector used to measure the output intensity so that a lossless switch should produce a transmission of 2. As in the transmission measurement of the SQW $\Delta\alpha$ switch, coupling losses from the facets were eliminated so that only the propagation losses through the switch are shown. The maximum transmission achieved was 97%, which is about one half of that required for a lossless switch in this measurement. This difference should be easy to correct by increasing the length of the gain sections, which are 100 μm long in this switch.

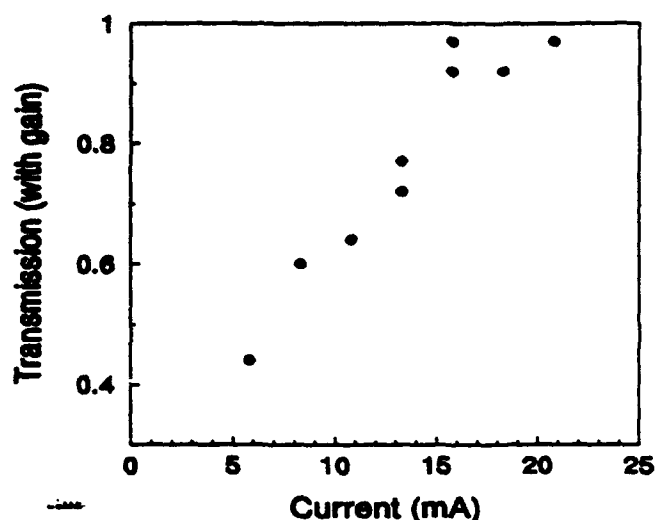


Figure 55. Measured transmission of the ACQW $\Delta\alpha$ switch as a function of current into each gain section. Measured intensity is from both switch outputs, facet losses are not included.

Reverse biasing of the bar and cross paths in this switch produced only weak modulation of the output. We believe this is because the disordering process destroyed the coupled well characteristics of the ACQW structure. With further experiments and modeling it will be possible to design quantum well structures that will have the desired ACQW characteristics after disordering.

8. Conclusions

8.1. Results

Both $\Delta\beta$ and $\Delta\alpha$ switches were fabricated and tested during this program. The $\Delta\beta$ switch with the ACQW structure is the most promising for a practical 2x2 cross-bar switch. Some experimental and modeling work is still needed to determine the initial quantum well structure necessary to give the required ACQW characteristics after the disordering process.

The $\Delta\beta$ switch, though asymmetric in its switching characteristics, can be used as a 1x2 switch with good transmission characteristics even without gain. Further, the techniques used to design the $\Delta\beta$ switch can be used to design

asymmetric coupled waveguides, which will couple only over a narrow wavelength band. These structures could be used for wavelength multiplexing. Since the waveguides in both switches were fabricated using the same processes, a larger device containing the $\Delta\alpha$ switch as well as the coupled waveguides could be fabricated using the techniques described here.

8.2. Possible Variations and Extensions

To produce a practical $\Delta\alpha$ switch, some additional changes can be made in the structure. The measurements with gain presented here were made using short duty cycle current pulses. This was required because the switches were not mounted on a heat sink. For continuous operation, as in a laser, the epitaxial side of the device must be bonded to a heat sink. For the multiple electrical contacts required for the $\Delta\alpha$ switch, this could be accomplished by depositing electrical conduction paths on a sapphire substrate. The switch could then be bonded to this substrate using standard indium bump hybridization. An added advantage of this would be that the electrical contact pads in the switch structure could be made much smaller than those used here. This would allow a narrower switch structure, which would require smaller turning mirror angles thus decreasing the loss in the turning mirrors.

Further work is also required in the areas of determination of the optimum gain section length and the design of the quantum wells for the VID process.

All the further work required to make a lossless $\Delta\alpha$ switch amounts to tuning of the structure presented here in. We are confident that with this additional effort a truly lossless switch can be fabricated using the ACQW structure with the vacancy induced disordering process.

9. References

1. R. P. Leavitt, J. W. Little and K. J. Ritter, "Feasibility Study of Resonant Tunneling Electro-Optic Quantum Well Devices," Final report contract #F19628-86-C-0059, MML TR 89-55C.
2. David Yevick and Bjorn Hermansson, "Spectral Analysis with Various Beam Propagation Techniques," J.Appl. Phys. 66, 5090 (1989).
3. D. Yevick, C. Rolland and B. Nermannson, "Fresnel Equation Studies of Longitudinally Varying Semiconductor Rib Waveguides: Reference Wavevector Dependence," Electron. Lett. 25, 1254 (1989).
4. D. Yevick and B. Hermansson, "Split-step Finite Difference Analysis of Rib Waveguides," Electron. Lett. 25, 461 (1989).
5. David Yevick and Bjorn Hermansson, "New Formulations of the Matrix Beam Propagation Method: Application to Rib Waveguides," IEEE J. Quant. Electron., 26,109 (1990).
6. J.A Fleck, J.R. Morris and M.D. Feit, "Time-Dependent Propagation of High Energy Laser Beams through the Atmosphere," Appl. Phys. 10, 129 (1976).
7. William H. Press, Brian P. Flannery, Saul A. Teukolsky and William T. Vetterling, *Numerical Recipes the Art of Scientific Computing* (Cambridge University Press, 1968).
8. D. A. B. Miller, D. S. Chemla, T. C. Damen, A. C. Gossard, W. Woegmann, T.H. Wood and C. A. Burrus, "Electric Field Dependence of Optical Absorption Near the Bandgap of Quantum-well Structures," Phys. Rev. B 32, 1043 (1985).
9. S. Somekh, E. Garmire, A. Yariv, H.L. Garvin, and R.G. Hunsperger, Appl. Optics, 13, 327-330 (1974).
10. Howard Appelman, Joseph Levy, Martin Pion, Danny Krebs, Charlton Harding and Mark Zediker, "Self-Aligned Chemically Assisted Ion-Beam-Etched GaAs/(Al,Ga)As Turning Mirrors for Photonic Applications," JLT 8, p.39 (1990).

DISTRIBUTION LIST

addresses	number of copies
ROME LABORATORY RL/EROC ATTN: RICHARD SOREF 80 SCOTT DRIVE HANSCom AFB MA 01731-2909	5
MARTIN MARIETTA LABORATORIES ATTN: DR. KENNETH J. RITTER 1450 SO. ROLLING ROAD BALTIMORE MD 21227	5
RL/SUL TECHNICAL LIBRARY 26 ELECTRONIC PKY GRIFFISS AFB NY 13441-4514	1
ADMINISTRATOR DEFENSE TECHNICAL INFO CENTER DTIC-FDAC CAMERON STATION BUILDING 5 ALEXANDRIA VA 22304-6145	2
ADVANCED RESEARCH PROJECTS AGENCY 3701 NORTH FAIRFAX DRIVE ARLINGTON VA 22203-1714	1

***MISSION
OF
ROME LABORATORY***

Mission. The mission of Rome Laboratory is to advance the science and technologies of command, control, communications and intelligence and to transition them into systems to meet customer needs. To achieve this, Rome Lab:

- a. Conducts vigorous research, development and test programs in all applicable technologies;
- b. Transitions technology to current and future systems to improve operational capability, readiness, and supportability;
- c. Provides a full range of technical support to Air Force Materiel Command product centers and other Air Force organizations;
- d. Promotes transfer of technology to the private sector;
- e. Maintains leading edge technological expertise in the areas of surveillance, communications, command and control, intelligence, reliability science, electro-magnetic technology, photonics, signal processing, and computational science.

The thrust areas of technical competence include: Surveillance, Communications, Command and Control, Intelligence, Signal Processing, Computer Science and Technology, Electromagnetic Technology, Photonics and Reliability Sciences.